

Final Report

Department of Transportation Phase I SBIR Contract Number: DTRT57-09-C-10046

Effective Date: August 20, 2009 through February 19, 2010;

Research Topic No. 091-PH1

Titled

Digital Imaging of Pipeline Mechanical Damage and Residual Stress

Prepared for

James Merritt
Department of Transportation
Pipeline & Hazardous Materials Safety Administration
Office of Pipeline Safety
(303) 683-3117
James.Merritt@dot.gov

Submitted by

David Jablonski, Ph.D., Principal Investigator
JENTEK Sensors, Inc.
110-1 Clematis Avenue
Waltham, MA 02453-7013
Tel: 781-642-9666
jentek@shore.net

February 19, 2010

These SBIR data are furnished with SBIR rights under Contract No. DTRT57-09-C-10046. For a period of 4 years after acceptance of all items to be delivered under this contract, the Government agrees to use these data for Government purposes only, and they shall not be disclosed outside the Government (including disclosure for procurement purposes) during such period without permission of the Contractor, except that, subject to the foregoing use and disclosure prohibitions, such data may be disclosed for use by support Contractors. After the aforesaid 4-year period the Government has a royalty-free license to use, and to authorize others to use on its behalf, these data for Government purposes, but is relieved of all disclosure prohibitions and assumes no liability for unauthorized use of these data by third parties. This Notice shall be affixed to any reproductions of these data, in whole or in part.

Preface

This final report provides the results and recommendations of the Phase I SBIR titled “Digital Imaging of Pipeline Mechanical Damage and Residual Stress”. Based on these results, JENTEK strongly recommends that a Phase II program or an additional follow-on contract is funded. This SBIR effort is critical to JENTEK’s commercialization plans for the detection and measurement of pipeline damage.

JENTEK has successfully completed the Phase I effort as described in the Executive Summary and in this final report. We appreciate this opportunity to contribute to the Department of Transportation’s Pipeline and Hazardous Materials Safety Administration progressive plans for improved safety of our nation’s pipelines by exploring new technologies that can detect damage and imminent failure in pipelines.

Table of Contents

1.0 Executive Summary

2.0 Work Plan and Technical Objectives

2.1 Phase I Technical Objectives

2.2 Phase I Work Plan

3.0 Summary of Phase I Results

3.1 Problem Definition

3.2 Simulation of pipeline mechanical damage with dented steel plates

3.3 Measurement of mechanical damage geometry and depth on steel plates

3.4 Finite element analysis of dented plates

3.5 Mapping of residual stress in dented steel plates

3.6 Relaxation of residual stress at a circular mechanical damage site

3.7 Measurements of mechanical damage on a 16 inch diameter pipe at RTD

3.8 Measurements of mechanical damage on a 24 inch diameter pipe at RTD

3.9 Changes of electromagnetic properties with strain of selected pipeline steel

1.0 Executive Summary

The purpose of this program was to enhance characterization of mechanical damage in pipelines through application of digital eddy current imaging. Lift-off maps can be used to develop quantitative representations of mechanical damage and magnetic permeability maps can be used to determine residual stress patterns around mechanical damage sites. Note that magnetic permeability is also affected by microstructure variations due to plastic deformation and plowing. High resolution digital images provide an opportunity for automated analysis of both size and shape of damage and a permanent archival record that can be compared against future measurements to detect changes in size or shape of the damage. Also, multiple frequency measurements will enable volumetric and even through-wall imaging at mechanical damage sites to support further risk assessment efforts.

The two major accomplishments of this Phase I SBIR were the development of methods to measure the geometry of pipeline mechanical damage using lift-off measurements with modified grids to correct for large scale geometry changes and the mapping of permeability around pipeline mechanical damage sites to characterize the residual stress state at these damage sites. To accomplish these objectives required the development of experimental techniques as well as selected experimental verifications of these techniques.

In this project, JENTEK, through laboratory testing, demonstrated techniques that can make accurate measurements of the pipeline mechanical damage geometry. To accomplish this, the sensor was mounted on a hard-backed plate for lift-off measurements. A finite element analysis was used to scale the measured MWM-Array lift-off measurements to provide accurate depth measurements. The scale factor was shown to be a function of dent diameter and dent depth. In the future, this correction factor could be built into the GridStation software so that the corrected lift-off values would be calculated and displayed.

The mapping of residual stress around a pipeline mechanical damage site requires that the sensor is mounted on soft-backed foam so as to conform to the pipeline surface. In addition, the measurement of the permeability at perpendicular orientations and the subsequent averaging of these two sets of measurements provide an improved mapping of the permeability changes around a pipeline mechanical damage site. In follow-on efforts, it is anticipated that a sensor that measures permeability at these two orthogonal directions and software that averages these measurements automatically could be developed to provide enhanced permeability mapping around pipeline mechanical damages sites.

The electro-magnetic properties of several steel plates were also measured for a variety of conditions. The measurements showed permeability increased with tensile strain and decreased with compressive strain. This was consistent with the permeability measurements made around mechanical damage sites such as dents. In the dented plates the center of the dent is in compression and the permeability was decreased from the baseline value. In the area adjacent to where the plates are supported during the denting process, the stress is tensile and the permeability is increased from the baseline value. We demonstrated that if these dented plates are annealed at a temperature of 650°C for 1-½ hours, the permeability approaches the values of the baseline un-dented specimen. However, there are still some geometric effects on the permeability values that are probably associated with the approach used to convert the sensor responses into effective properties. Future work could develop a procedure for compensating for these geometric effects on the permeability values.

2.0 Work Plan and Technical Objectives

2.1 Phase I Technical Objectives

1. Demonstrate the feasibility of delivering a “low-cost, time-efficient, reliable, and simple to use” product that is commercially viable.
2. Determine the relationship between electromagnetic properties of pipeline steels and stress, including hysteresis behavior and temperature effects.
3. Investigate methods to improve spatial resolution of lift-off and permeability.
4. Investigate methods to improve the measurement of residual stress around mechanical damage in pipelines.

2.2 Phase I Work Plan

Task 1. Problem definition.

Task 2. Acquire materials for mechanical damage specimens.

Task 3. Determine electromagnetic properties of selected pipeline steel.

Task 4. Acquire or fabricate mechanical damage specimens.

Task 5. Perform computer simulations to assess potential performance of candidate designs.

Task 6. Perform laboratory testing to determine capabilities of candidate approaches.

Task 7. Investigate feasibility of enhancing spatial resolution of mechanical damage geometry images.

Task 8. Evaluate correlation of permeability measurements with residual stresses.

Task 9. Final report.

3.0 Summary of Phase I results

3.1 Problem Definition

The basic types of mechanical damage in pipelines include dents and gouges, or a combination of both as shown in Figure 1. In addition to these basic types of mechanical damage, cracks may be present in the dents or gouges. In some cases the dent may not be very visible because it has been re-rounded by the internal pressure in the pipe, thus making these types of mechanical damage very difficult to detect. This type of damage should show up as an area of high residual stress due to the deformation done in the mechanical damage event and the re-rounding with internal pressure. We did locate a number of pipeline samples with mechanical damage for this program; however we did not have any samples that had re-rounding of the dents. One goal would be to estimate the size of the mechanical damage prior to re-rounding to support risk assessment efforts.

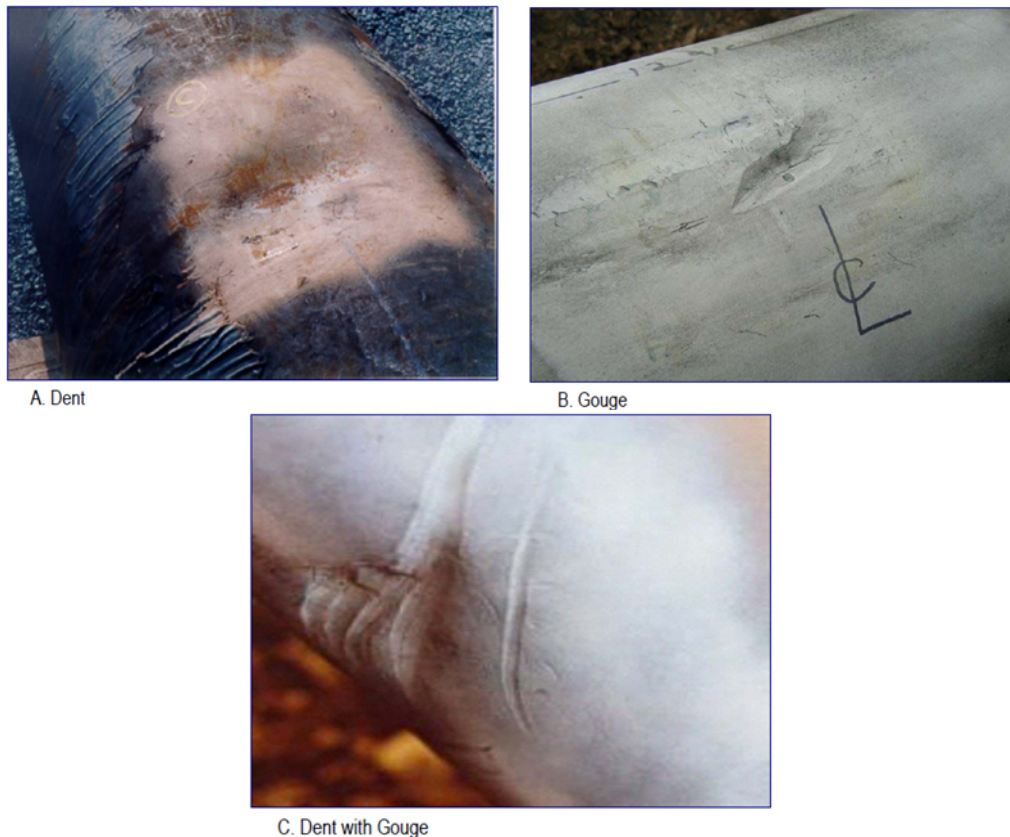


Figure 1. Examples of mechanical damage in pipelines [Baker, 2009]

The mechanical damage due to dents can be characterized by measuring the dent depth, “h”, and then dividing by the outside diameter of the pipe, “d” and multiplying this by 100 to obtain a percentage.

$$\text{Dent damage (\%)} = (h/d) * 100$$

The size at which a dent is characterized as a repair or replacement action depends upon which standard is used (i.e., API 1156, ASME B31.8, EPRG, PDAM or CZ662) and also on the individual requirements of the pipeline operators. In general, dent damage greater than 6% of the pipeline outside diameter (OD) is considered large enough to warrant either a repair action or a replacement action. If this dent is located on the weld, then the damage can only be 2% of the pipeline OD. Dent depths that require either repair actions or replacement actions are listed in Table 1 for typical pipeline sizes.

Table 1. Dent depths that require repair or replacement actions in pipelines

Pipe OD (in.)	Plain Dent Depth(in.)	Dent in Weld(in.)
6	0.36	0.12
12	0.72	0.24
18	1.08	0.36
24	1.44	0.48
30	1.80	0.60
36	2.16	0.72
46	2.76	0.92

This large range of dent depths that must be detected and characterized (based upon pipe size) may require different sensors to accommodate the range of dent sizes that must to be detected and measured.

3.2 Simulation of pipeline mechanical damage with dented steel plates

JENTEK has simulated mechanical damage due to dents in flat plates of 4130 steel using a procedure similar to that used by Clapham². We chose to simulate dents in the range that would require either a repair or replacement action for 6-inch, schedule 40, 10 or 5 pipes. We obtained flat plates of 4130 steel in the annealed condition with thicknesses that are approximately equal to wall thicknesses of schedule 40, 10 and 5 pipes. These plates which were 0.25, 0.125 and 0.080 inches in thickness were cut to a 6-inch by 6-inch size and indented with a hardened steel ball with either 25/32 inch (~20 mm) diameter or 1.575 inch (~40mm) diameter steel ball. The setup for making this dent is shown in Figures 2 to 4. The base that the steel plates rested on had a 3-inch diameter hole (see Figure 3). The amount of indentation was controlled by measuring the displacement of the hydraulic ram with a dial indicator, as shown in Figure 4. The final dent size obtained by this method is less than the value indicated on the dial indicator, since this deflection is also affected by the elastic deflections of both the plate and press structure. After some initial experiments, with an existing fixture provided with the press, produced unsymmetrical deformation, we developed a special fixture that allowed us to produce symmetric deformation.

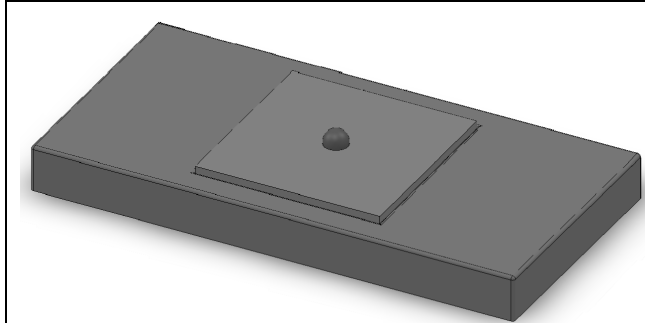


Figure 2. CAD rendering of fixture used to dent plates for mechanical damage simulation

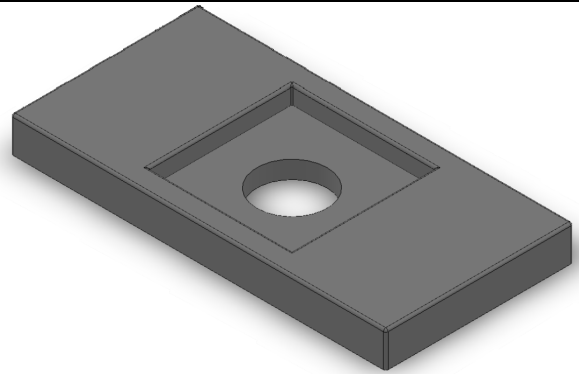


Figure 3. CAD rendering of lower plate showing 3 inch diameter hole that supports the plate to be dented for mechanical damage simulation



Figure 4. Hydraulic press with fixtures used to dent plates to simulate pipeline mechanical damage.

We selected 3 different standard sensor designs. All 3 sensors can be used for scanning to obtain lift-off and permeability maps for these steel plates. The sensors we used were the FA24, FA26 and FA28, which are shown in Figures 5 to 7. The FA28 sensor has relatively small dimensions and is useful for very high spatial resolution images of the material condition. In contrast, the FA24 and FA26 sensors have larger dimensions and are better suited for creating high spatial resolution images with moderate stand-off distances or lift-offs.

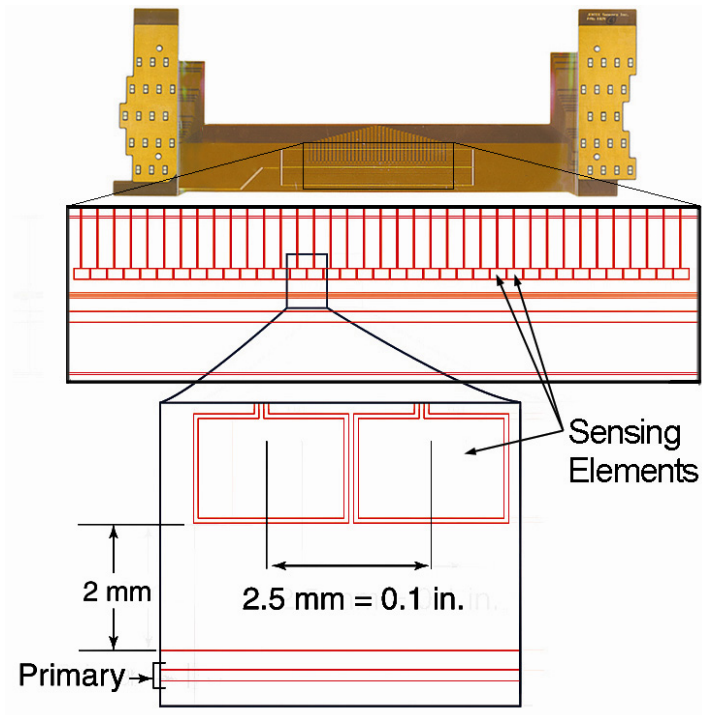


Figure 5. FA24 MWM-Array sensor.

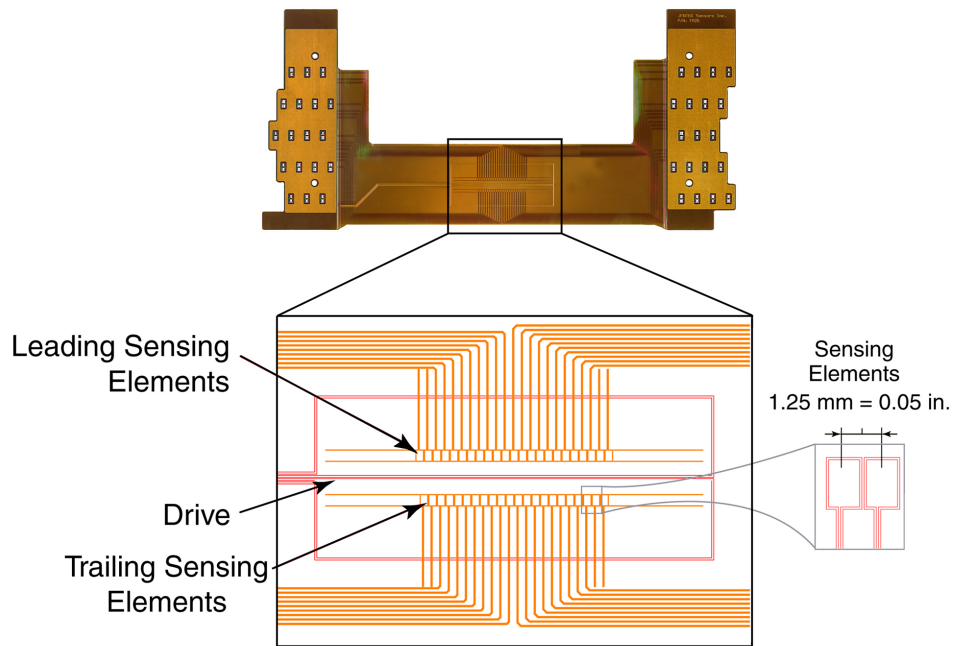


Figure 6. FA26 MWM-Array sensor.

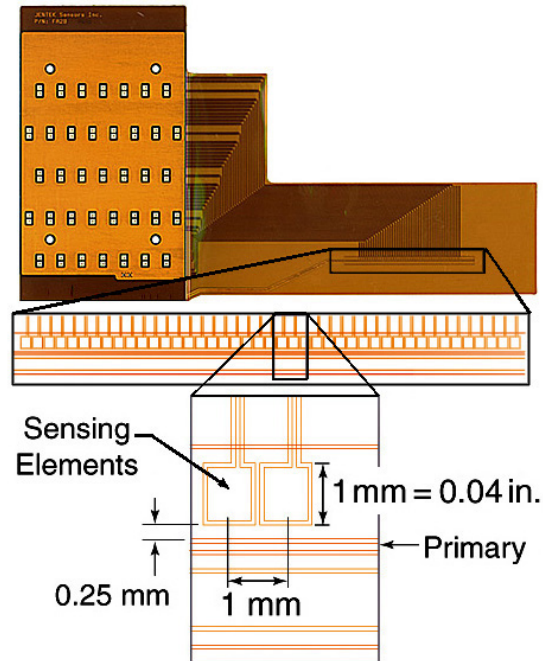


Figure 7. FA28 MWM-Array sensor.

The FA24 and FA26 sensors have the same drive winding to sense element spacing of 0.0878 inches (2 mm), but the sense element is twice as long for the FA24 (0.1 inches) versus 0.05 inches for the FA26. The FA28 has a smaller sense element to drive winding spacing of 0.01 inches and a smaller sense element length of 0.04 inches. After measuring the size of the mechanical damage, we determined that the FA28 sensor could not accommodate the large amount of lift-off for these specimens, so we concentrated on the FA24 and FA26. The FA26 sensor showed better sensitivity to spatial property variation because the sense elements are smaller.

The test setup for scanning the plates is shown in Figures 8 and 9. The sensors are mounted on a probe unit, and there is either a layer of foam between the sensor and the probe, or a rigid piece of plastic between the probe unit and sensor. The use of soft foam allows the sensor array to better conform to the surface geometry of the dent and permits relative permeability measurements relatively close to the indentation site; the use of a hard backing or a rigid shim is better for providing depth profile estimates across the entire damage area. When the intent of the measurement was to measure the geometry and depth of the mechanical damage site, a hard backed sensor was used. When the intent was to map the residual stress through permeability measurements a soft foam backed sensor was used. The results of these two separate types of measurements are presented separately.

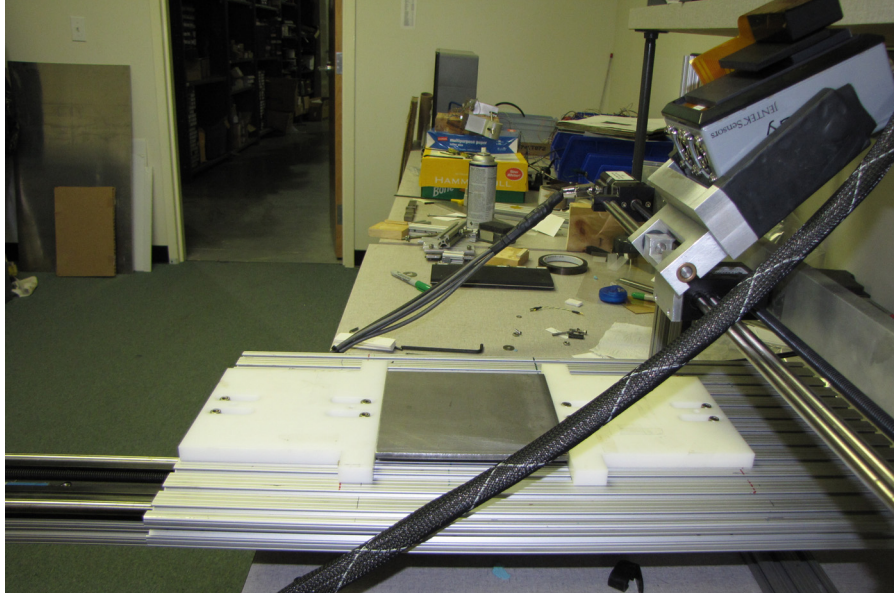


Figure 8. Test setup used to scan dented steel plate showing FA-26 MWM-Array mounted on soft foam.



Figure 9. Test setup to scan dented steel plate with MWM-Array.

3.3 Measurement of mechanical damage geometry and depth on steel plates

A significant portion of this program was focused on developing procedures for the measurement of mechanical damage on steel plates, with the understanding that the use of the flexible MWM-Arrays could be applied to materials with curvature as well. For this portion of the effort, measurements were performed on ¼-inch thick plates. We chose 5 plates (see Table 2) on which we have made detailed lift-off and permeability measurements. The first 3 plates; T4R4, B4R4 and T1R1 were indented using a 0.782-inch (20 mm) diameter steel ball and indented to displacements of 0.30, 0.20 and 0.10 inches as measured by the dial indicator, respectively. The actual depth of the damage was less than the dial indicator value because of the elastic spring back, once the pressure was released. The last 2 plates, B4L4 and T4L4, were indented using a 1.575-inch (40 mm) diameter steel ball to displacements of 0.30 and 0.20 inches, respectively.

Table 2. Summary of plates that were dented and annealed

Plate Number	Ball diameter	Press indentation
T4R4	0.782 in. (20mm)	0.30 in.
B4R4	0.782 in. (20mm)	0.20 in.
T1R1	0.782 in. (20mm)	0.10 in.
B4L4	1.575 in. (40 mm)	0.30 in.
T4L4	1.575 in. (40 mm)	0.20 in.

All of these plates were scanned on JENTEK’s 2D scanner using an FA26 MWM-Array sensor. In all of these scans, a control plate without dents was also scanned; the C-scans for the control plate are shown on the left side of all the C-scans that are presented in Figures 10-21. For scans on the front side of the dent, the FA26 sensor was mounted on a hard plastic backing to get accurate lift-off measurements. For the scans on the back side of the plate, the FA26 sensor was mounted on soft foam backing so the sensor conforms to the protrusion from the dent. For each plate we measured the dent depth at the centerline of the dent with a digital dial indicator. After all these measurements were made, the plates were annealed in a furnace at 550°C for 4 hours and these measurements were repeated. These measurements used an air-shunt calibration. The measurement data was converted into effective permeability and lift-off values using measurement grids, as described below.

Figures 10 through 21 show the lift-off images from these plates on both the front and back sides. These measurements were made before and after annealing the plates. The annealing process did not change the lift-off images, so we have only shown the lift-off image after annealing for only one plate. The lift-off images after annealing for the other plates are available, but they are not shown in this report since they do not offer any additional value.

As expected, the lift-off images show larger lift-off values as the press indentation is increased. The lift-off images do not change after annealing which indicates the dent geometry did not change and, since the annealing should only affect the permeability values. **The use of measurement grids provides independent estimates of the lift-off and permeability values.** This result was confirmed by comparing the lift-off measurements with the dial indicator before and after the plates were annealed.

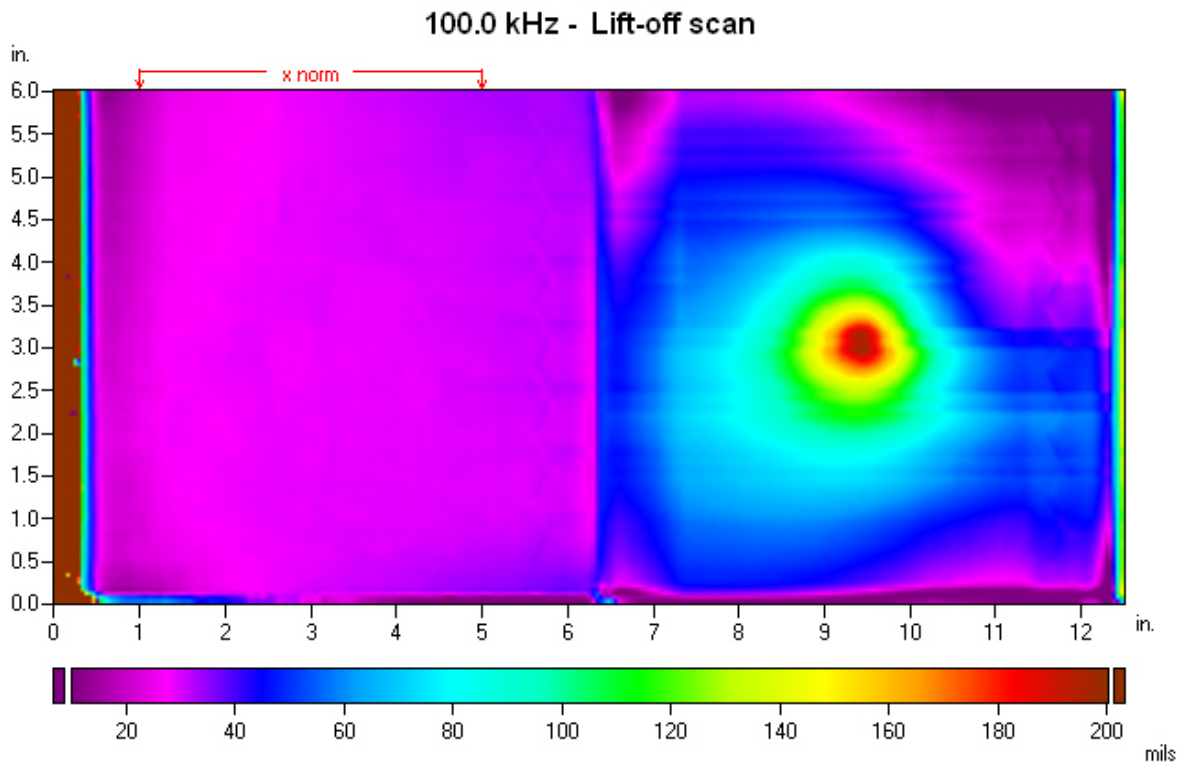


Figure 10. Lift-off C-scan images for the control plate (left) and T4R4 front side (right): condition as dented.

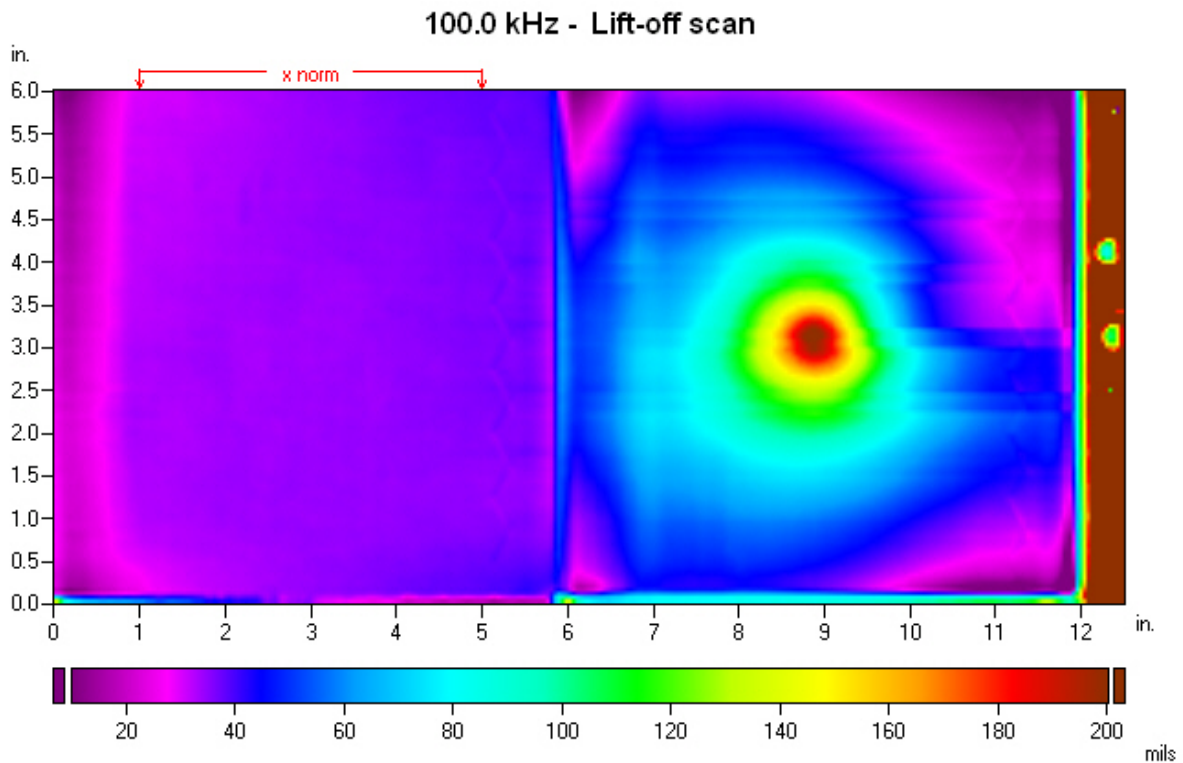


Figure 11. Lift-off C-scan images for the control plate (left) and T4R4 front side (right): condition as annealed.

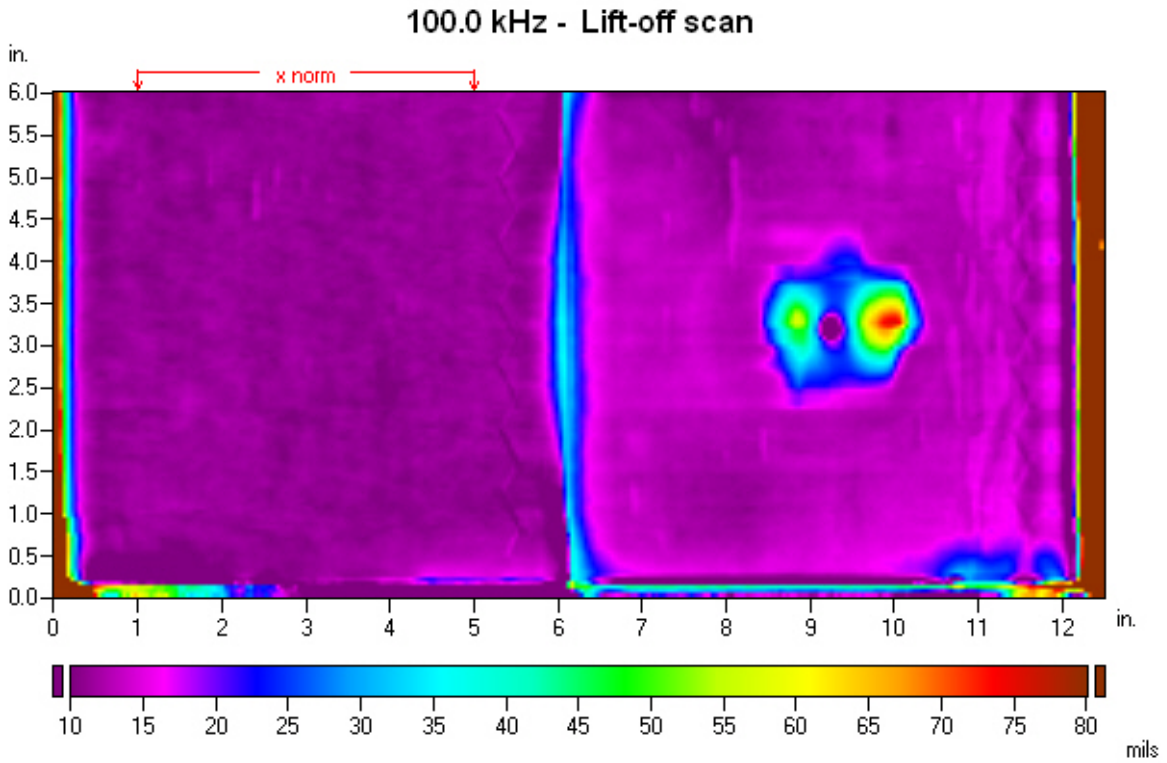


Figure 12. Lift-off C-scan images for the control plate (left) and T4R4 back side (right): condition as dented.

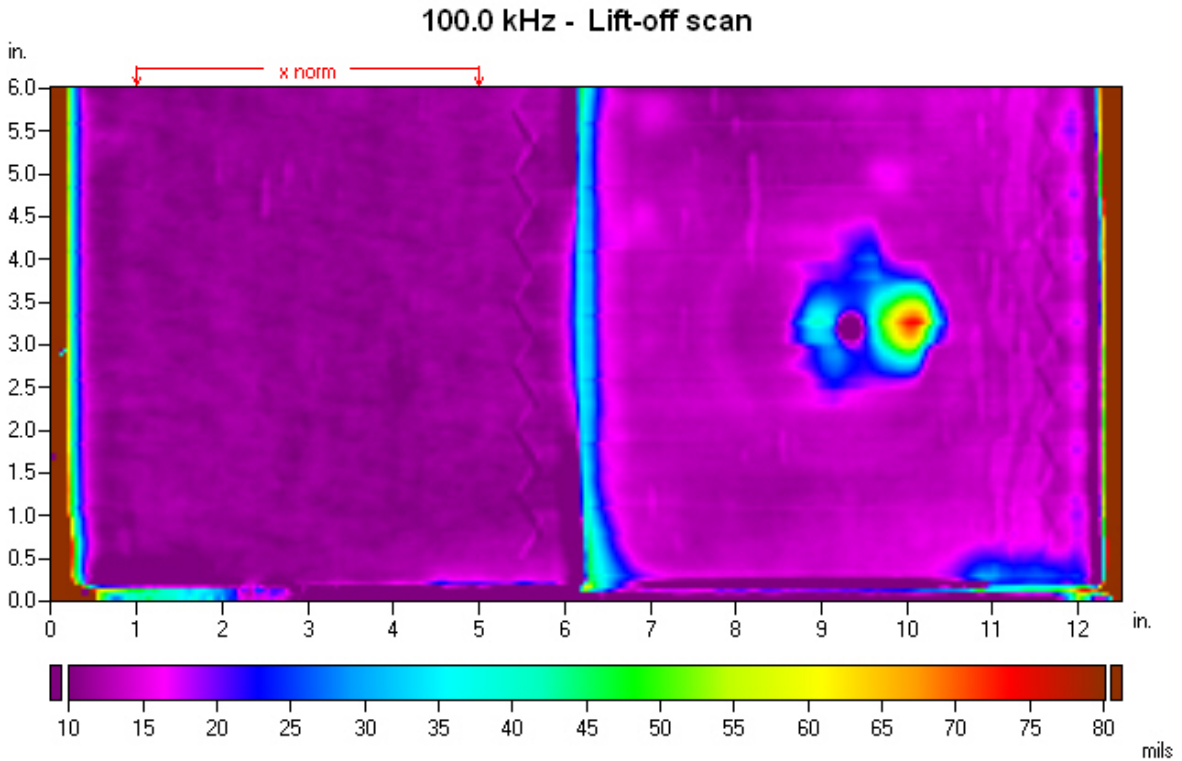


Figure 13. Lift-off C-scan images for the control plate (left) and T4R4 back side (right): condition as annealed.

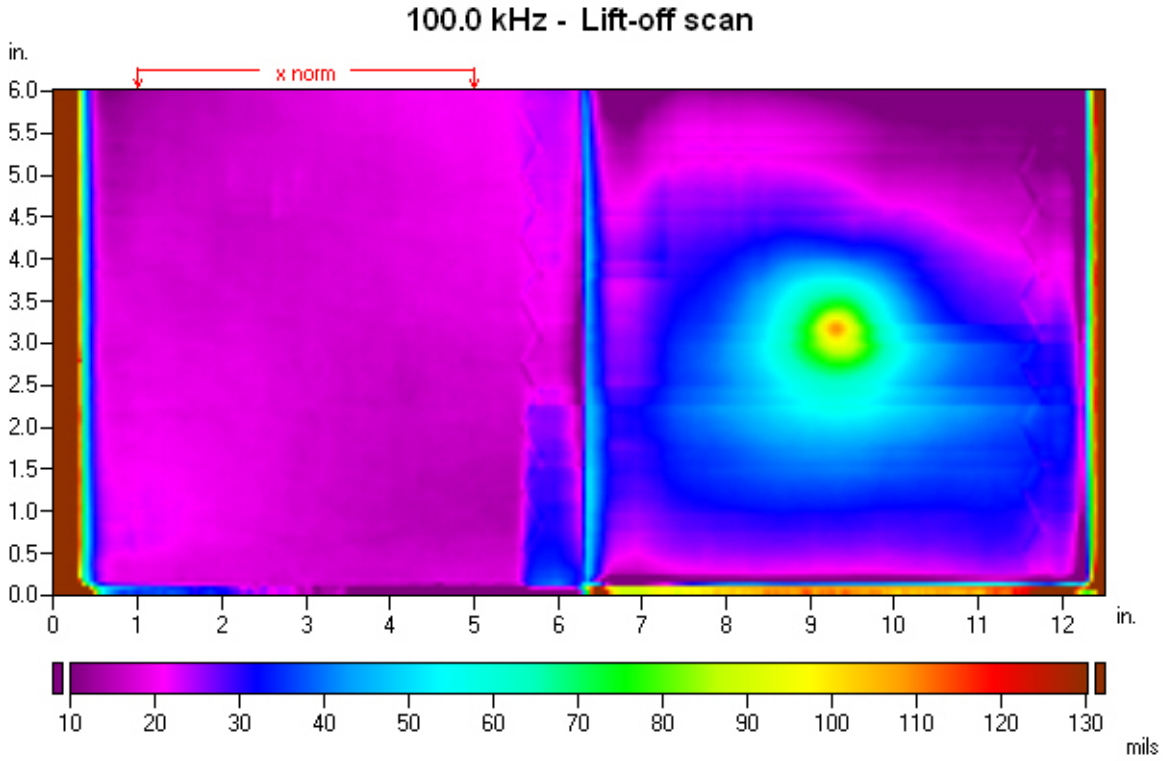


Figure 14. Lift-off C-scan for B4R4 front side: condition as dented.

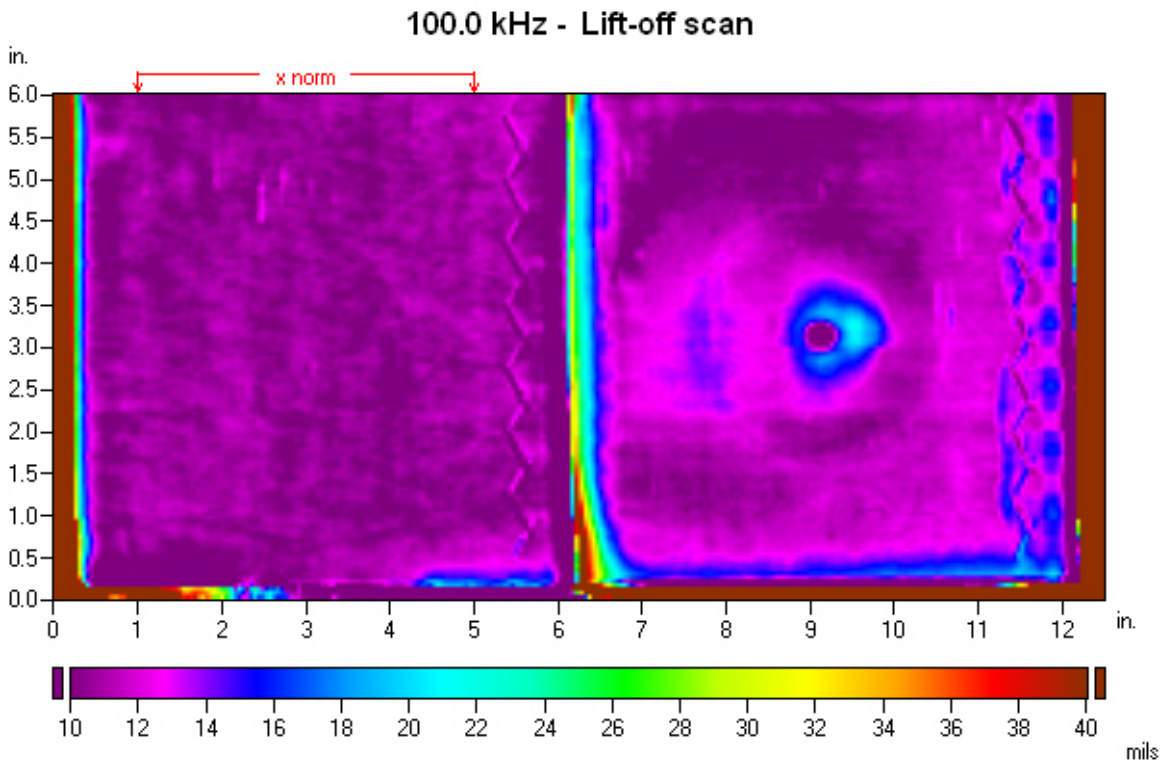


Figure 15. Lift-off C-scan for B4R4 back side: condition as dented.

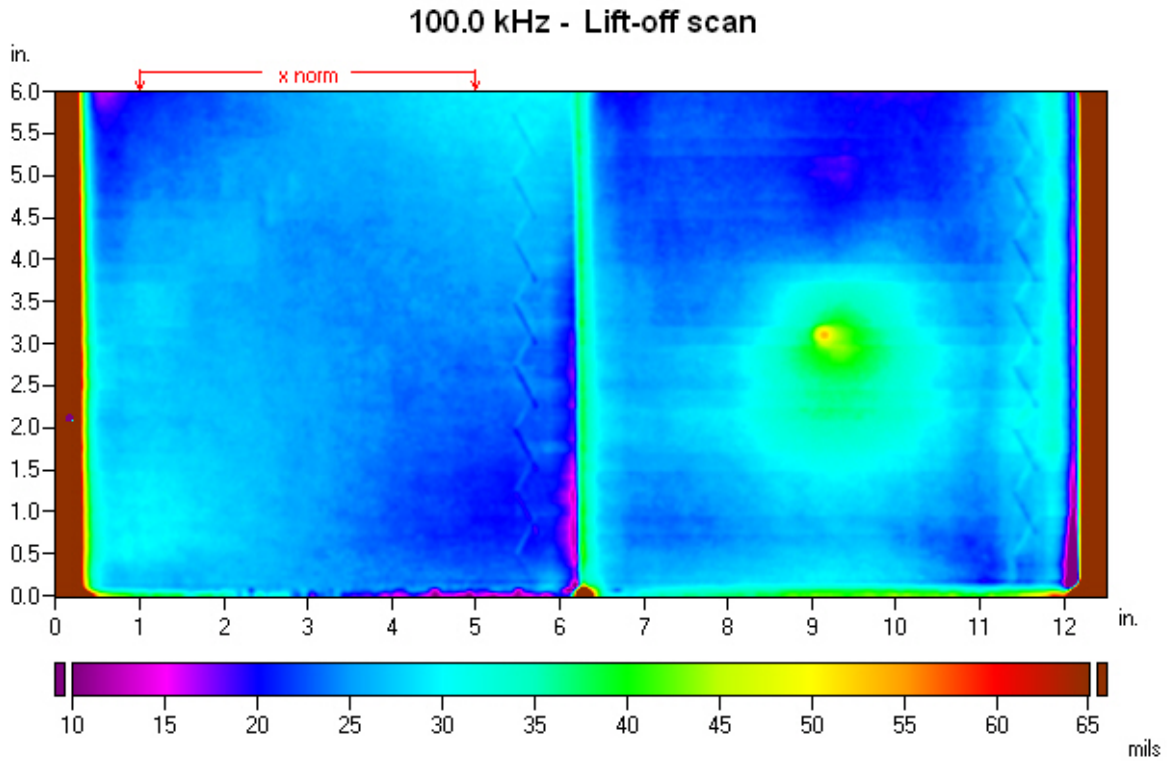


Figure 16. Lift-off C-scan for T1R1 front side: condition as dented.

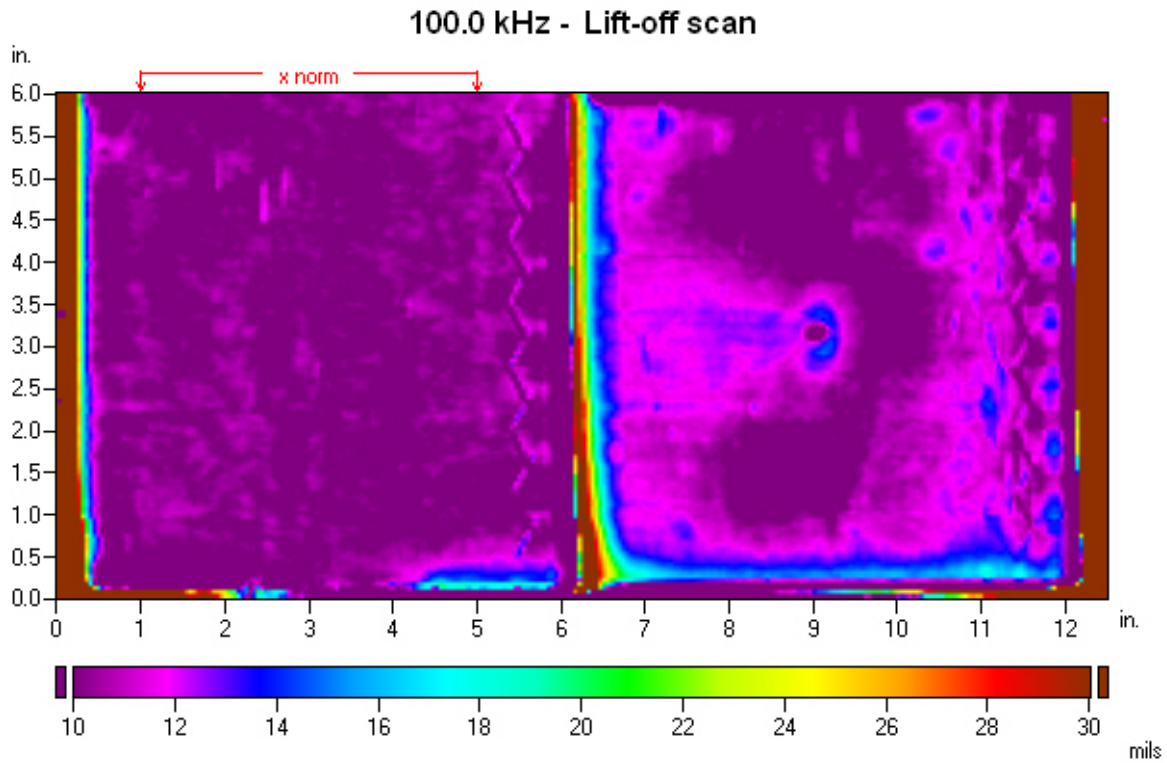


Figure 17. Lift-off C-scan for T1R1 back side: condition as dented.

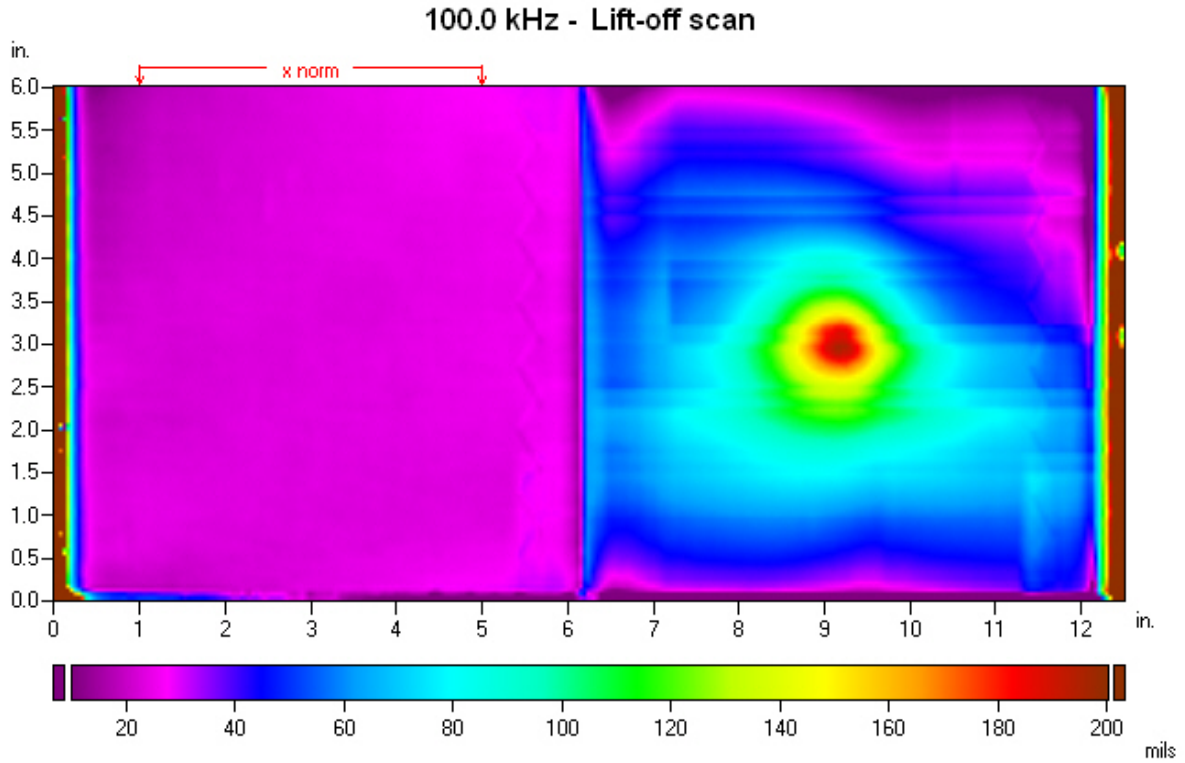


Figure 18. Lift-off C-scan for B4L4 front side: condition as dented.

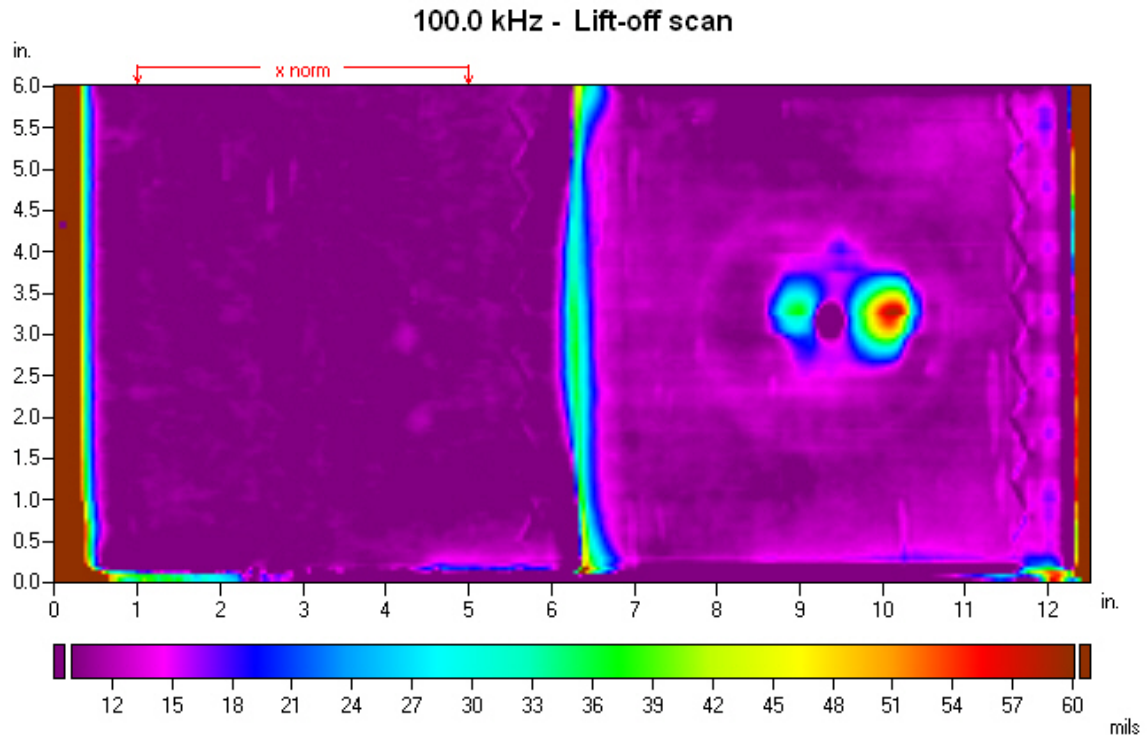


Figure 19. Lift-off C-scan for B4L4 back side: condition as annealed.

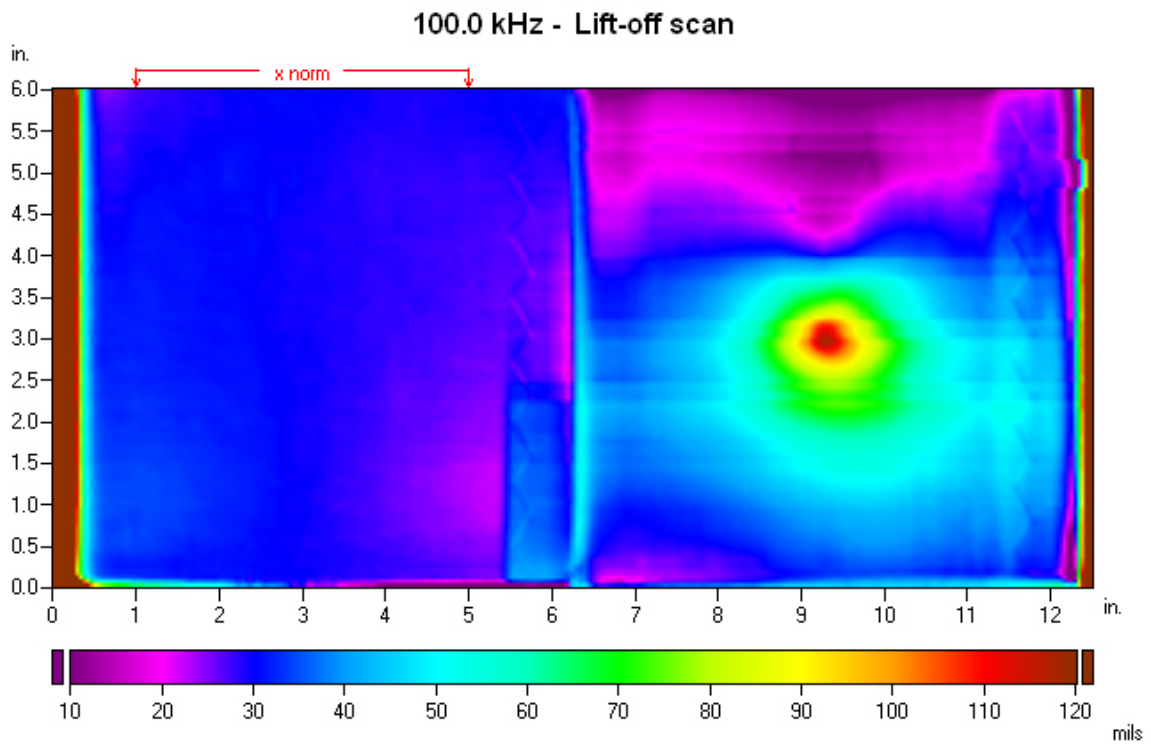


Figure 20. Lift-off C-scan for T4L4 front side: condition as dented

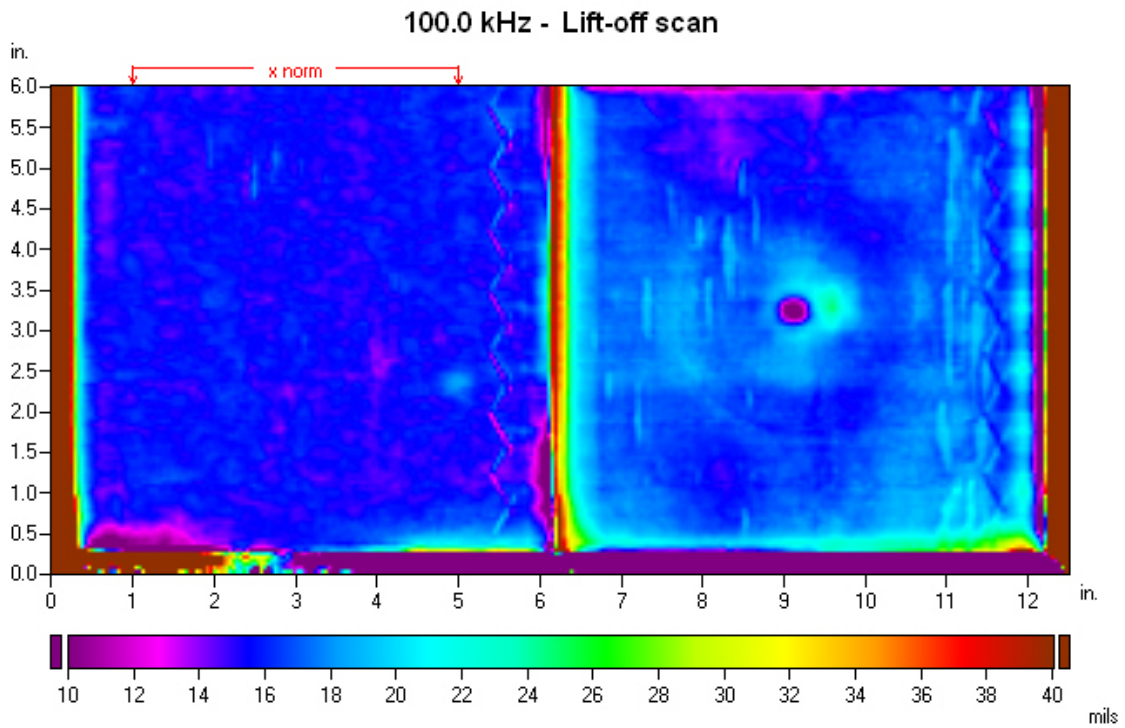


Figure 21. Lift-off C-scan for T4L4 back side: condition as dented

A comparison of the dent depths as measured by the digital dial indicator is shown in Figure 22. The dent depth is primarily controlled by the deflection imposed by the hydraulic press. Changing the indenter ball from 0.782 to 1.575 inch diameter has very little effect on the depth of the dent.

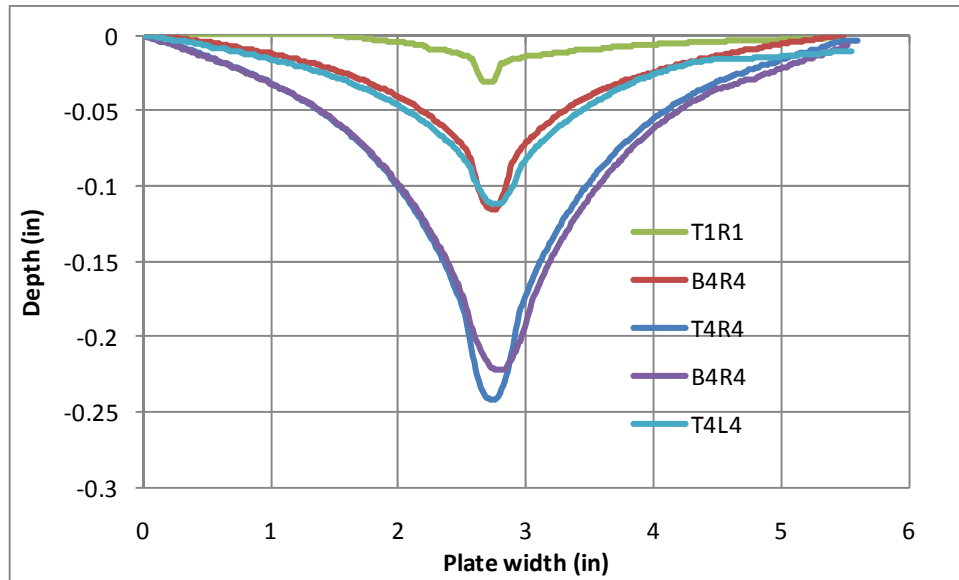


Figure 22. Dent depths as measured by the digital indicator for all 5 plates tested.

We also made comparisons between the lift-off B-scans at the center line of the dent to the measurements made with the digital dial indicator. The experimental setup to measure the depth with the dial indicator is shown in Figure 23.

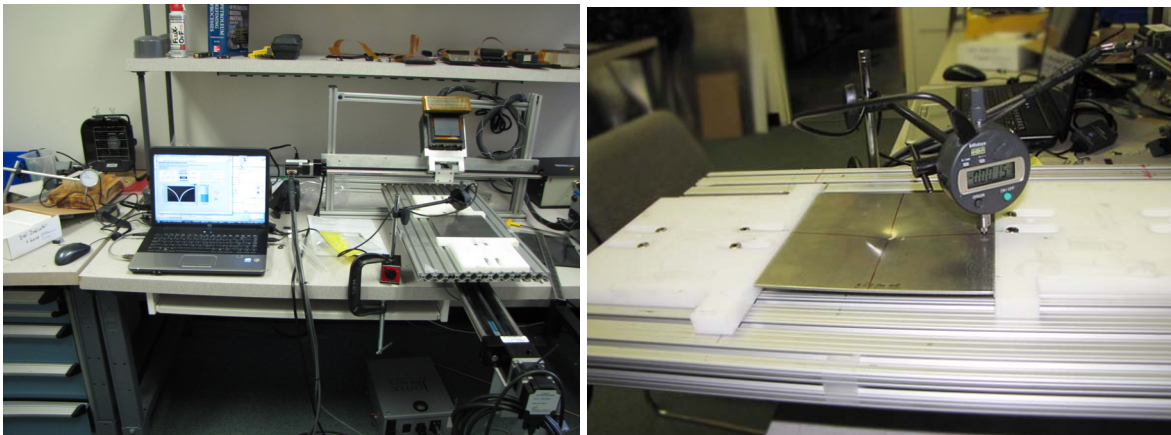


Figure 23. Photos of setup used to measure dent profile with a digital dial indicator.

To accurately compare the MWM-Array lift-off measurements to those from the digital dial indicator, the sensor lift-off from the steel plates surface was corrected to subtract any lift-off due to both the shim used and any air gap caused by non-uniform bending of the plate. These results are shown in Figures 24 to 27. In all cases, as expected, the MWM-Array measured lift-off is less than the depth measured by the digital dial indicator. The measurement grid used to convert the impedance to lift-off and permeability assumed that the part has uniform planar layers with constant properties. This allows the grids (pre-computed databases) to be generated rapidly using the late Prof. James Melcher's layered media formulas. In the case where the layers are not uniform, but curved as in the dented samples, these assumptions break down

and the models are not as accurate. These curvature effects can be incorporated into the models, but the equations are much more complex and require finite element simulation to generate the corrected grids. The next section describes finite element results for a locally curved plate that simulates the plates we used in our experiments. As will be seen later, these results suggest that a scaling factor can be applied to the lift-off values to correct for the non-planar layer assumption.

Also shown in the plots in Figures 24 to 27 are scaled lift-off values, which simply mean the measured lift-off was multiplied by a constant factor. For plates T4R4 and B4L4, which had dents of approximately the same depth, we used a scale factor of 1.55, and for plates B4R4 and T4L4 which had shallower dents of approximately the same size, we used a scale factor of 1.35. Once these scaling factors are applied to the lift-off measurements, they agree with the results from the digital dial indicator. These scale factors were empirically determined by finding the best fit of the lift-off measurements to the dial indicator measurements. Later a finite element simulation was performed to calculate these scale factors from the geometry changes. As shown in the next sections, the empirically determined scale factors were the same as those calculated with the finite element analysis.

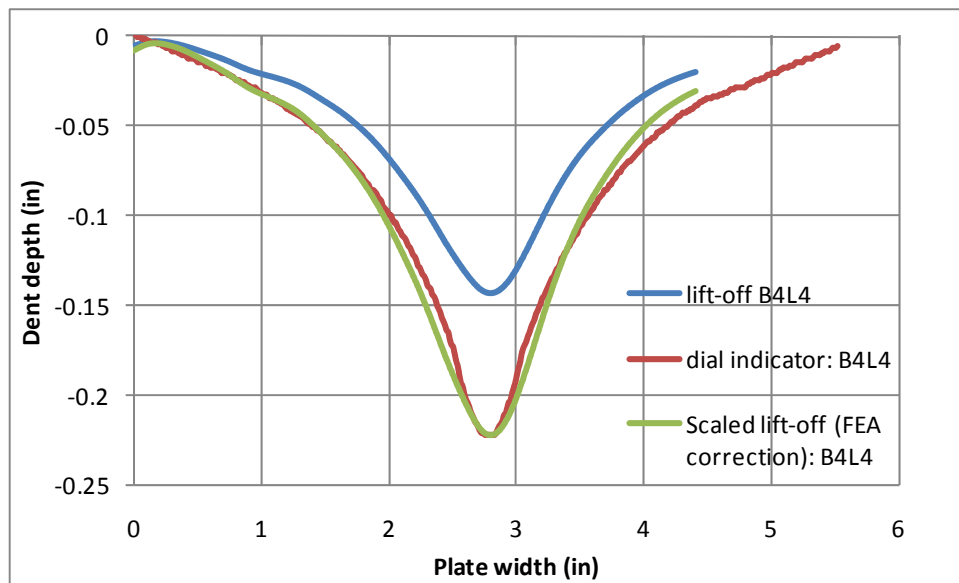


Figure 24. Dent profiles for plate B4L4 based on lift- dial indicator measurements and scaled lift-off (scale factor 1.55).

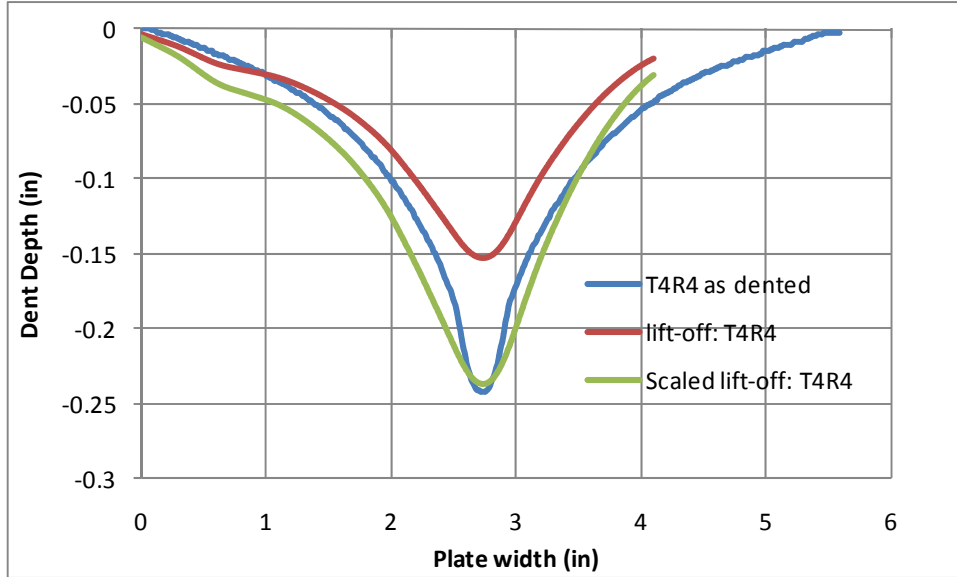


Figure 25. Dent profiles for plate T4R4 based on lift- dial indicator measurements and scaled lift-off (scale factor 1.55).

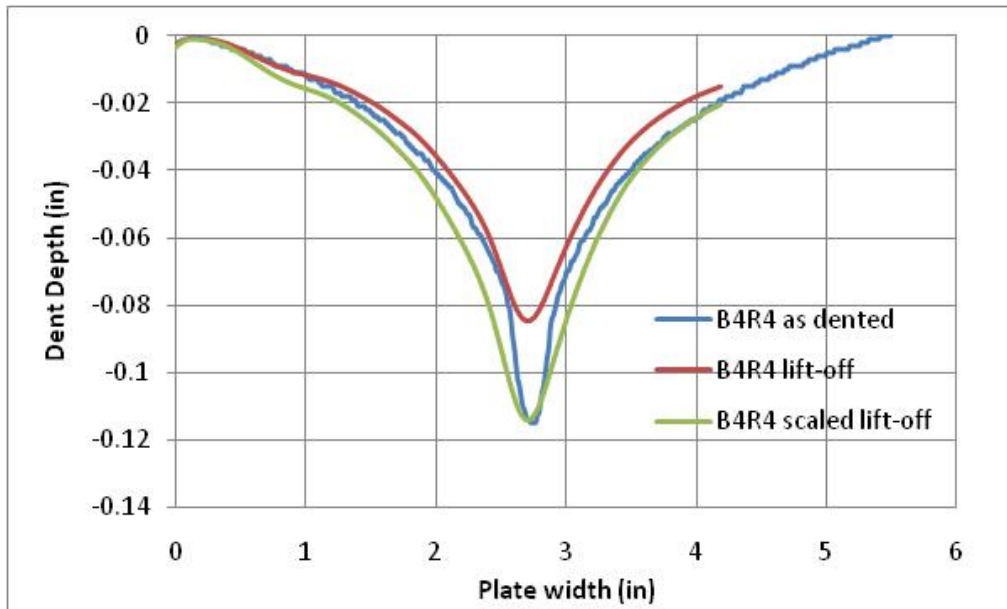


Figure 26. Dent profiles for plate B4R4 based on lift- dial indicator measurements and scaled lift-off (scale factor 1.35).

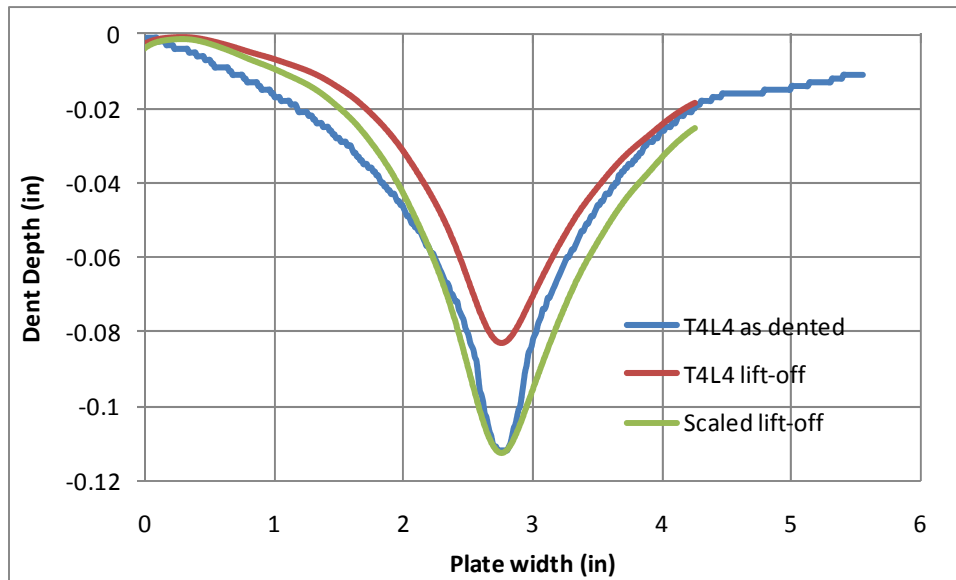


Figure 27. Dent profiles for plate T4L4 based on lift- dial indicator measurements and scaled lift-off (scale factor 1.35).

3.4 Finite element analysis of dented plates

A series of simulations were performed to determine the effect of the geometry changes associated with mechanical damage, such as dents on the effective property estimates of an MWM-Array. In this case, the geometry of Figure 28 was assumed. Due to symmetry, only a quarter of the geometry needed to be solved in the model calculation. An FA26 sensor was centered over a dent in a 6.35 mm thick steel plate. The upper surface of the plate was then deformed to simulate the presence of the dent; for the relatively high excitation frequencies considered here, of 10 or 100 kHz, the inspecting magnetic field from the sensor does not penetrate through the thickness of the plate and the sensor responds to near-surface properties in the plate. The dent itself contained a flat central section of diameter 5.08 mm and a larger area of deformation where the depth varied linearly from the surface to the central section. The FA26 sensor response was calculated as the depth of the central section and the diameter of the larger region were varied. The responses were processed using standard permeability/lift-off measurement grids to yield effective material properties. The nominal properties of the steel plate were a relative permeability of 40 and an electrical conductivity of 3.75%IACS. A nominal lift-off of 0.762 mm (0.030-in.) was assumed to simulate inspecting through a rigid plate.

Figure 29 shows the predicted change in effective lift-off as the depth and diameter of the dent are varied. This change in the effective lift-off is calculated by estimating the lift-off with the flaw present and subtracting the nominal lift-off; this yields an estimate of the depth of the dent itself. In general, for large dent diameters and shallow depths, the change in the material geometry is small and the predicted lift-off change is in rough agreement with the actual depth. However, for large depths and for small dent diameters, the predicted change in lift-off is smaller than the actual depths. This indicates that the measured, effective lift-off changes need to account for the geometry changes in order to yield a reasonable dent depth estimate. The simplest way to do this correction is to scale the measured response using the ratio of the predicted to actual depths either from Figure 30 or from empirical measurements on a series of plates dented to different depths.

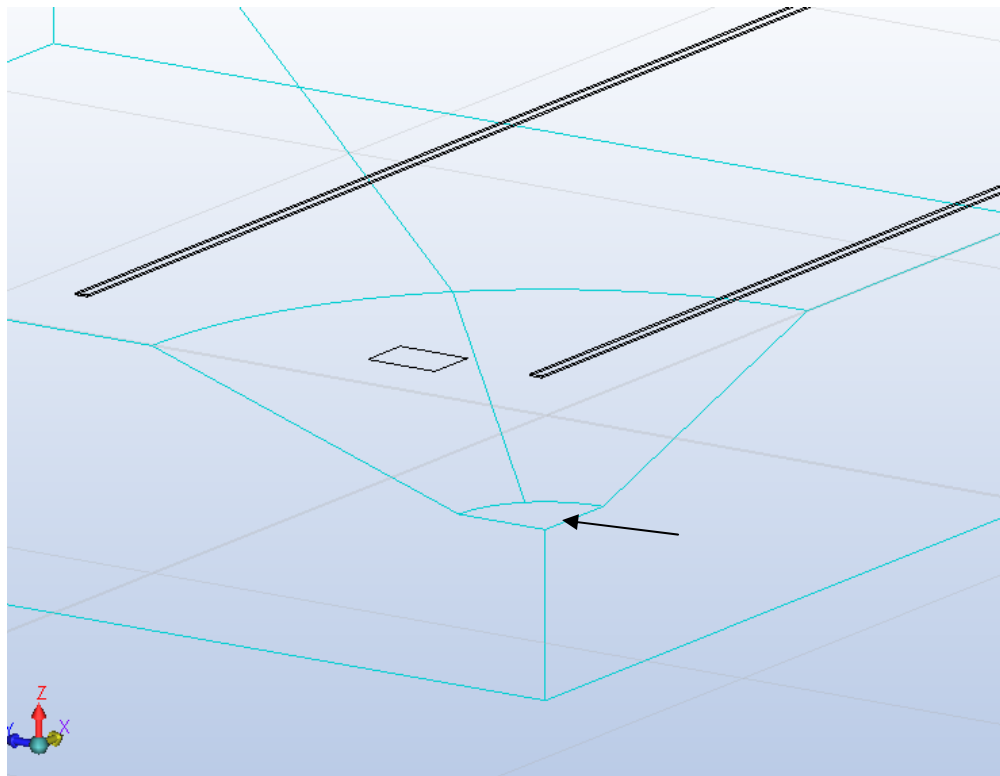


Figure 28. Quarter-section of the model geometry for an FA26 sensor centered over a dent in a steel plate.

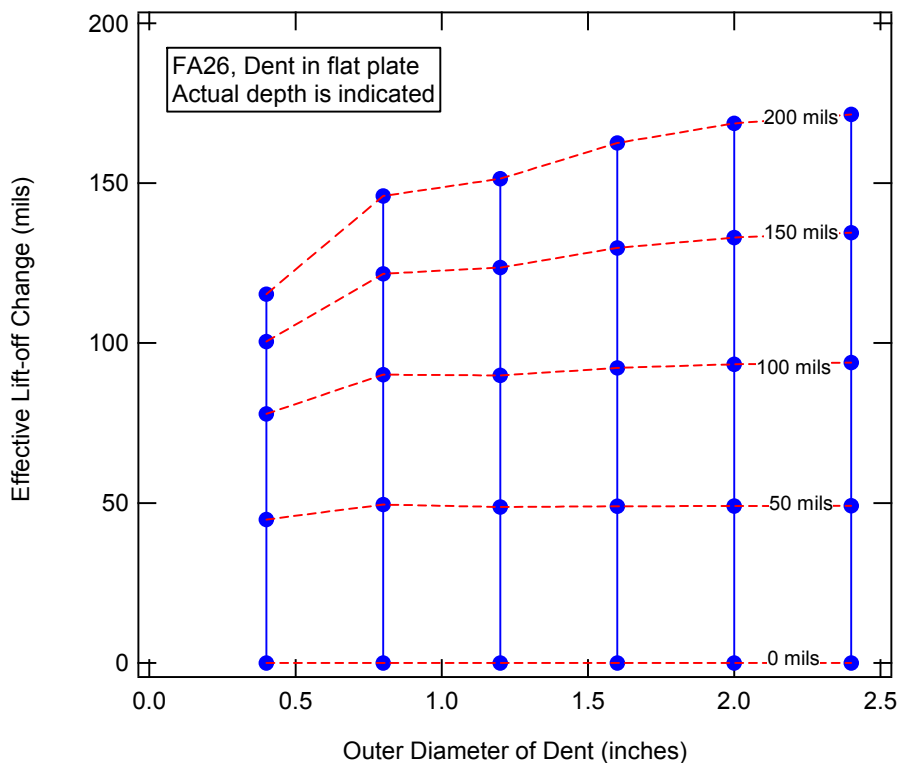


Figure 29. Predicted change in effective lift-off as the diameter and depth of a dent in a flat plate are varied.

Figure 30 shows the predicted lift-off correction factor to compensate for geometric effects on the lift-off estimate for the dent depth. These curves were obtained from the data of Figure 29 and indicate how the correction factor changes with the width and depth of the dent. For a shallow dent, the correction factor is near one, which indicates that the lift-off value provides a good estimate of the dent depth. However, for deep and narrow dents, the correction factor can be significant.

In Figure 30, the T4R4 and B4R4 plates had dents ~ 200 mil in depth and the diameter of ~ 0.60 inches. From Figure 30 the scale factor is 1.55, which is what we found empirically for the data. Also in Figure 30, for plates B4R4 and T4L4, the dents were ~ 110 mils in depth and the diameter was ~0.40 inches. Again using Figure 30 the scale factor is 1.35, which is what we found empirically for the data. These calculated correction factors and our experimental measurement confirm that **accurate dent depth and geometry can be made using MWM-Arrays and grids corrected for the non-planar geometry** that occurs in a pipe with mechanical damage.

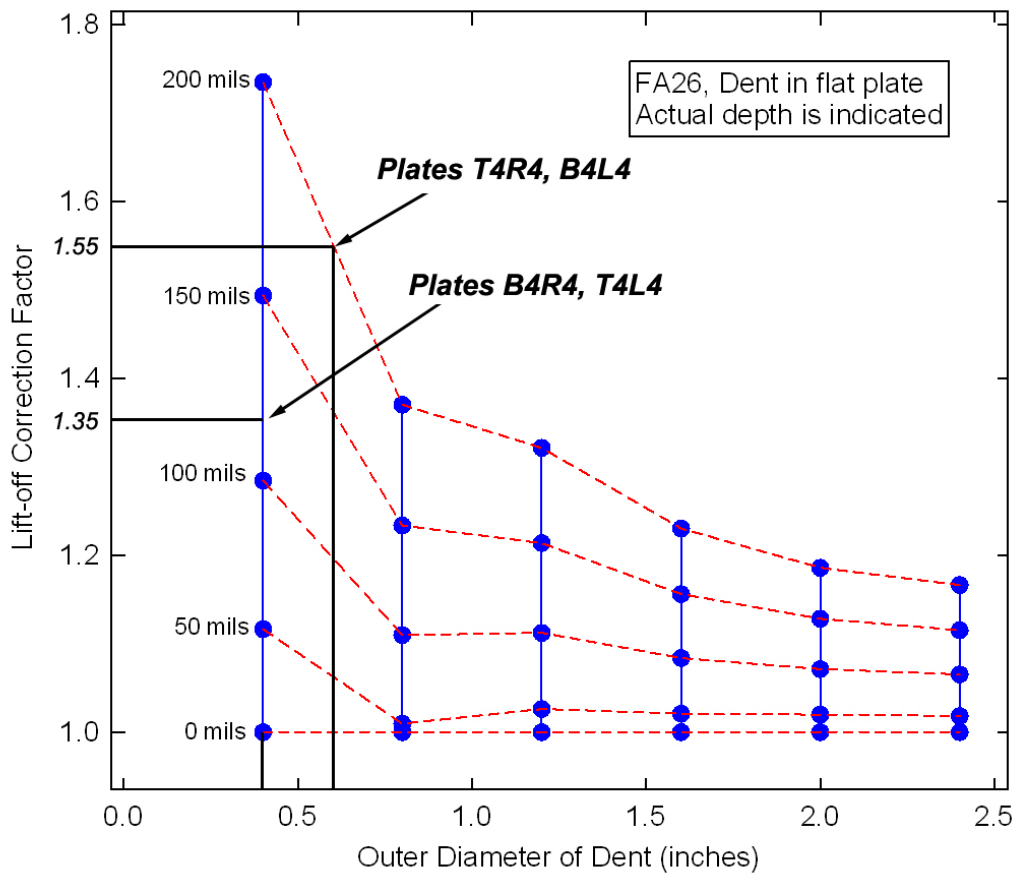


Figure 30. Predicted lift-off correction factors to compensate for the geometry effect on the lift-off estimate.

3.5 Mapping of residual stress in dented steel plates

Figure 31(a) shows three images of MWM-Array measured permeability of a circular mechanical damage site. The image on the left and center are images of the magnetic permeability in two orthogonal directions. The image on the right is the averages of these two images (at each pixel), and, since the magnetic permeability of steels is known to vary with stress, this image provides a measure of the residual stress at that location. A relative increase in the magnetic permeability for this material represents an increase in tensile stresses (or an increase in susceptibility to stress corrosion cracking or fatigue crack initiation and growth).

Figure 31(b) shows the three lift-off (surface topology, or *magnetic profilometry*) images corresponding to the same images for two orthogonal directions and averaging these images. The lift-off images are the same for all two directions (as expected) while the permeability (or residual stress) shows directional properties.

Figure 32 provides photographs of the loading frame used for sample preparation and MWM-Array scanning test setup and JENTEK GridStation system with the probe and MWM-Array (flexible eddy current sensor). Figure 33 provides an illustration of the two MWM-Array drive winding orientations (of course in the test setup the part is rotated, not the sensor). Note that in follow-on efforts a V-shaped MWM-Array could be fabricated that has an integrated + and – 45 degree angle drive with separate sensing element arrays to enable data capture in a single pass.

Figure 34 provides an interesting visualization of these results. The JENTEK grid methods, using measurement grids (pre-computed databases) such as shown in Figure 34 (top left), enable independent imaging of the surface topology (using magnetic profilometry) while at the same time in the same scan an image of the magnetic permeability (residual stress pattern) is provided. As shown in Figure 34 (middle left), the surface topology is extremely smooth as intended, but, the residual stresses are highly varied (middle right). The pattern that shows a decrease in permeability at the center of the dent and then an increase in the permeability approximately 1 inch from the dent center is consistent with finite element simulations from the literature by Clapham [2]. These finite element simulations show that the stress is compressive in the center of the dent and gradually transitions to tension away from the dent and then back to a state of zero stress at a larger distance from the dent center. Our results show a slightly more complicated stress state. We believe that the method used to make the dents did introduce a more complex stress state, because the part was supported too close to the indentation to allow a smooth transition of the residual stresses. This resulted in the more complex response shown in the permeability B-scans. This is an exciting and somewhat unexpected result. Thus, in continuing work, we will modify the denting process to produce various patterns of surface topology and residual stress variations. We also plan to model the elastic-plastic behavior to understand the mechanical denting process itself. Note that this data was taken through a 0.03 in. insulating layer, to demonstrate inspection through thin coatings.

Note from the data in Figure 34, even though the very smooth surface topology image (from the magnetic profilometry) can accurately measure the dimensions of a mechanical damage site, it is most interesting that local stress concentrations can occur even when the surface topology variation is more gradual. This is critical for assessment of mechanical damage sites. In follow-on efforts, we hope to analyze these stress patterns and even run fatigue tests to demonstrate the correlation between these patterns and both static strength reduction and fatigue damage evolution from various mechanical damage sites. This ability to perform rapid magnetic profilometry and residual stress imaging has the potential to provide significantly new inspection and characterization capabilities. While the work to date has been limited to near-surface analysis, on-going work aimed at development of a low frequency measurement capability with solid-state sense elements should be able to provide near-surface profilometry, wall thickness and *volumetric (3-D) residual stress imaging, in relatively thick pipeline walls (up to 1 in.)*.

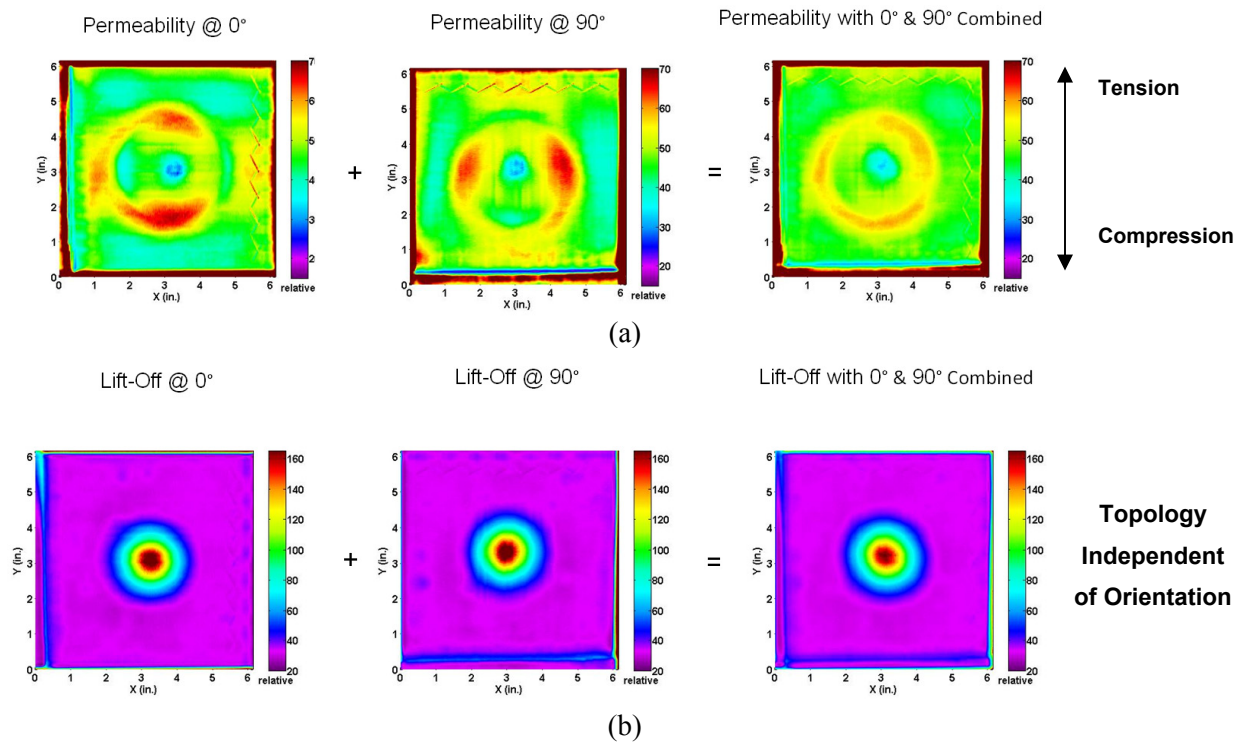


Figure 31. (a) Three images of a circular mechanical damage site. The image on the left and center are images of the magnetic permeability in the perpendicular and parallel directions relative to the scan direction. The image on the right is the average of these two images (at each pixel), providing a measure of the residual stress at that location. Note that this data was taken through a 0.03-in. insulating layer, to demonstrate inspection through coatings. **(b)** The three lift-off (surface topology or *magnetic profilometry*) images corresponding to the same orthogonal and averaged images as in Figure 31(a). As you can see, the lift-off images are the same (as expected) while the permeability (or residual stress) shows directional properties.

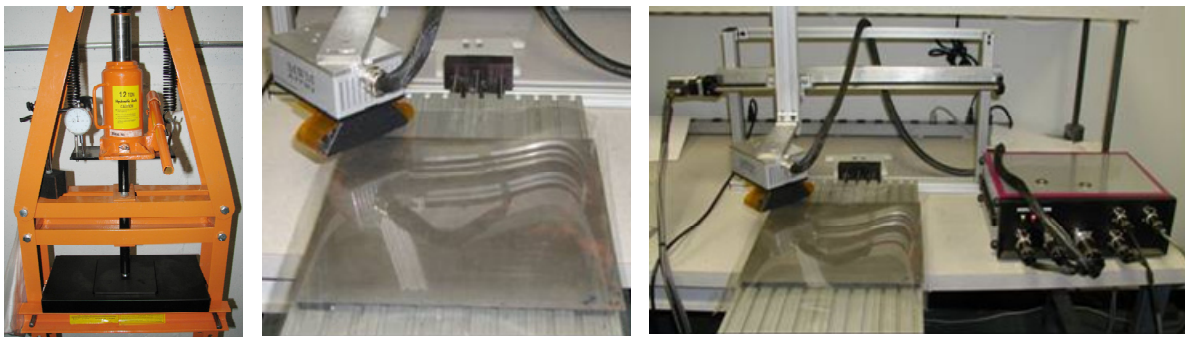


Figure 32. Photographs of the load frame used for sample preparation, test measurement setup, and the JENTEK GridStation System with the probe and MWM-Array.

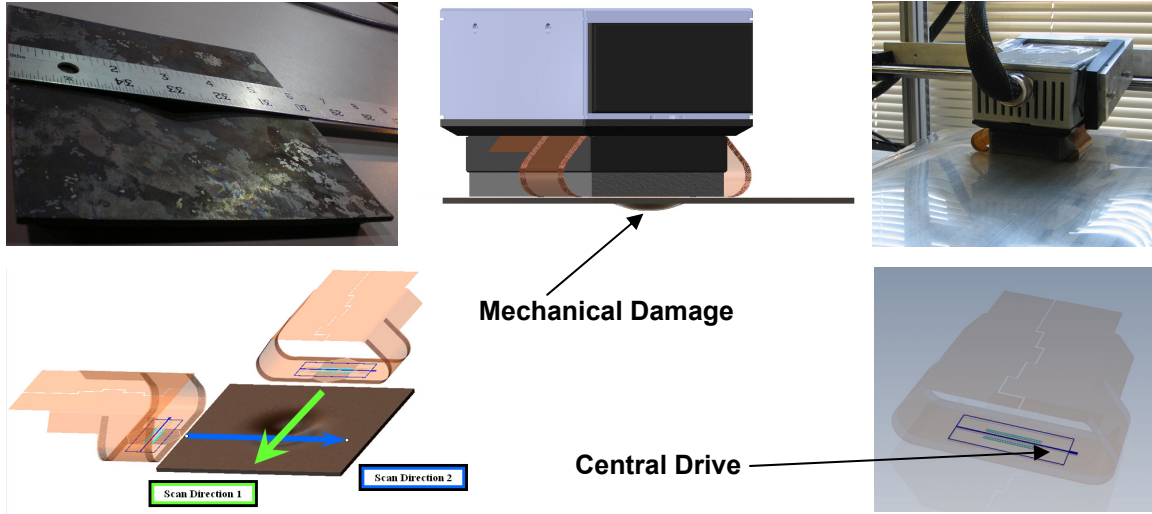


Figure 33. Illustration of the MWM-Array drive winding orientation during scanning with the drive in the two orthogonal orientations.

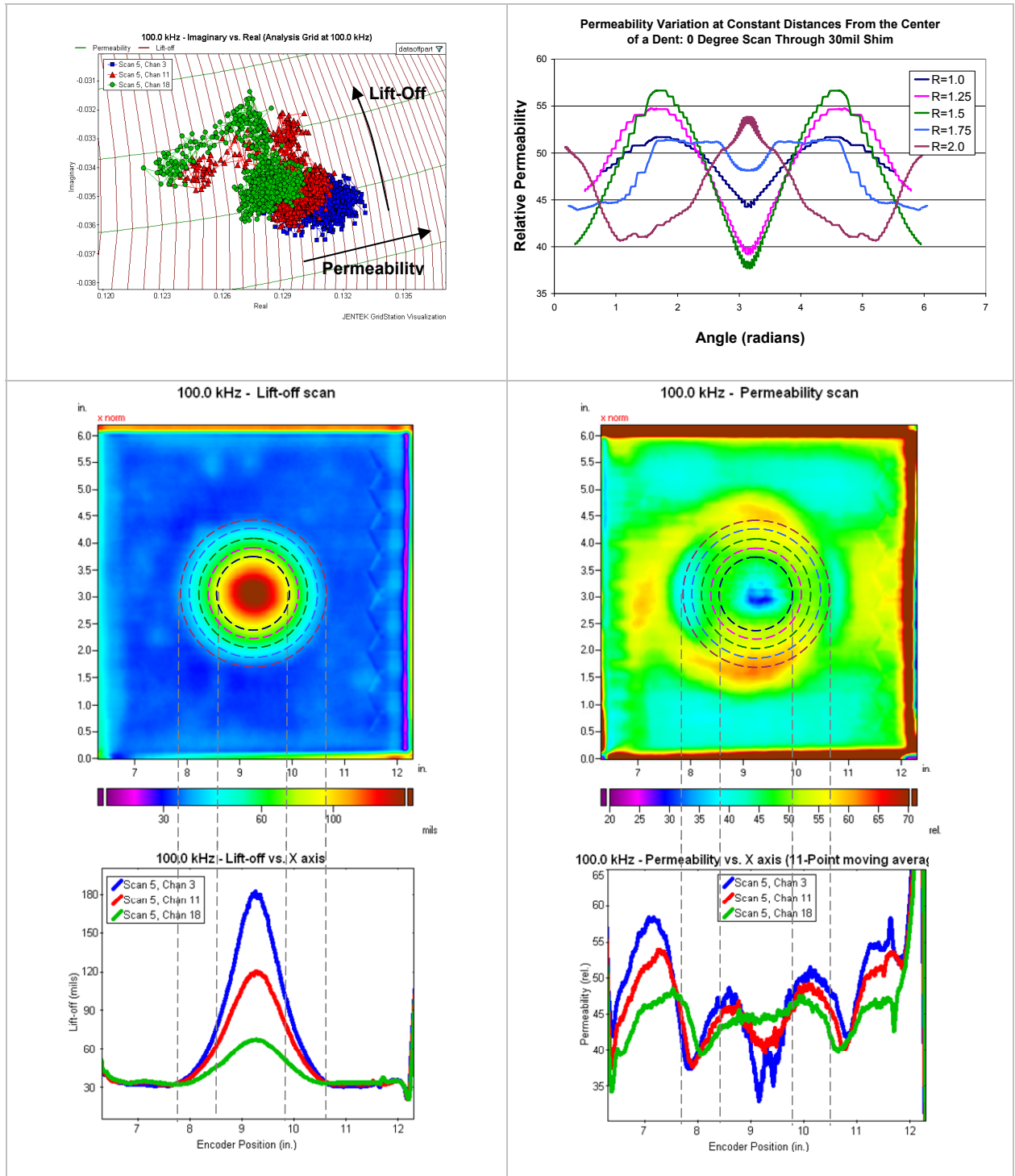


Figure 34. Top Left: JENTEK measurement grid (the grid methods enable independent imaging of the surface topology and magnetic permeability at the same). Middle Left: The lift-off (surface topology) image. Bottom Left: B-Scan of surface topology. Top Right: Changes in permeability at constant radii from the center of the dent. Middle Right: The magnetic permeability image (the dotted circles are of varying radius from the center of the dent). Bottom Right: B-Scan of magnetic permeability.

The results presented in Figure 31 show that a more accurate measurement of the permeability change and residual stress around a mechanical damage site can be obtained by averaging the 0° and 90° permeability images obtained in orthogonal orientations around a mechanical damage site. We investigated use of additional orientations around the mechanical damages site by making measurements at +45° and -45° orientations. These are shown in Figure 35, with the averaged images shown in Figure 36. Clearly there is a slight improvement by averaging all four orientations, but the improvement is marginal compared to the use averaging of two images at orthogonal orientations from each other.

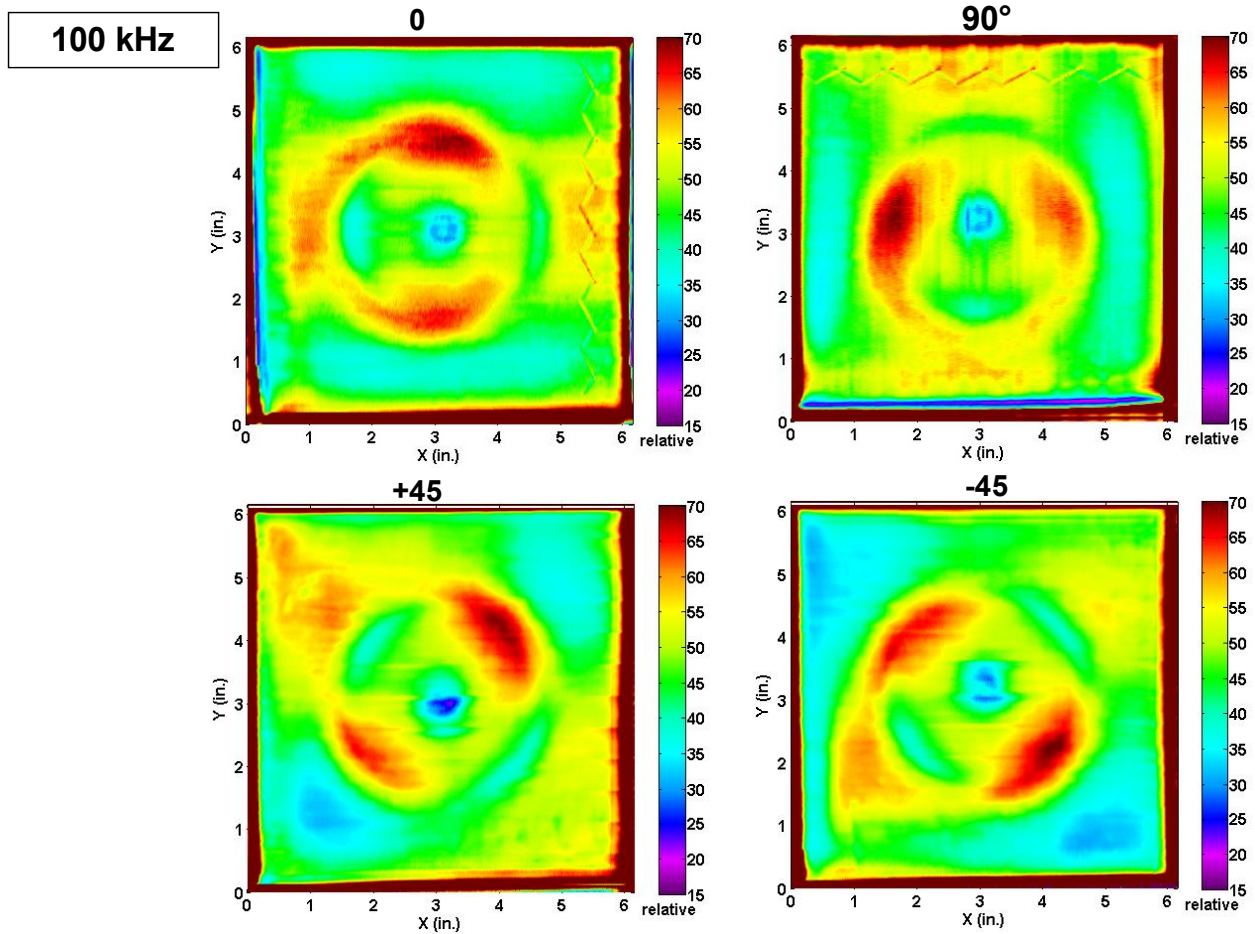


Figure 35. Four permeability images obtained by scanning circular mechanical damage site in different orientations. The top two images were obtained by scanning in the 0° and 90° orientations and the bottom two images were obtained by scanning in the 45° and -45° orientations.

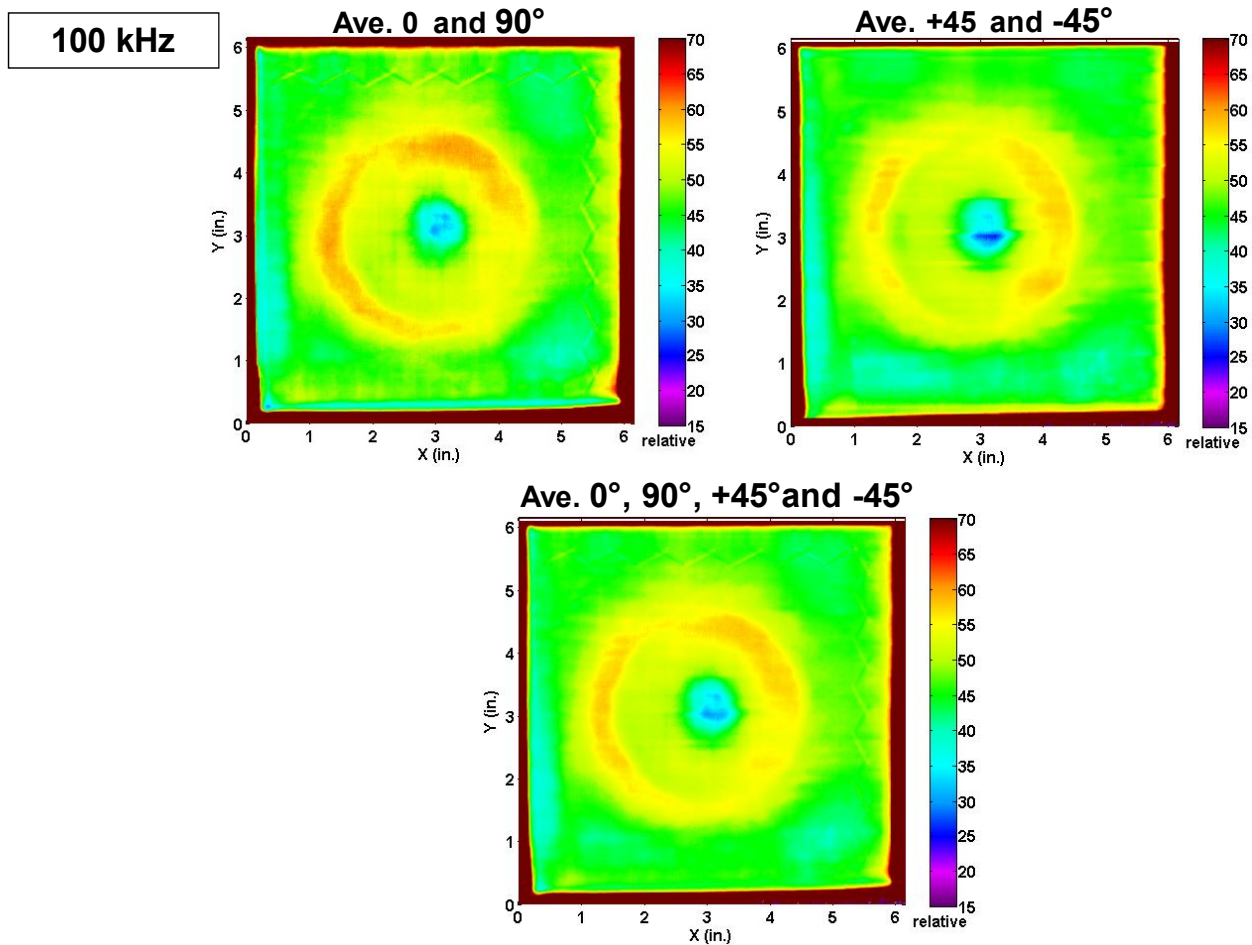


Figure 36. Top left: averaging of 0° and 90° permeability images for a circular mechanical damage site; Top right: averaging of 45° and -45° permeability images for a circular mechanical damage site; and Bottom: averaging of 0°, 90°, 45° and -45° permeability images for a circular mechanical damage site.

3.6 Relaxation of residual stress at a circular mechanical damage site

The previous section reported on an experimental technique to obtain a more accurate measure of the residual stress (i.e. permeability variation) around a symmetric mechanical damage site by averaging permeability images at 0° and 90°. For the previous section, measurements were not made on the plate before annealing, so it was difficult to quantify the effect of annealing. Consequently we repeated some of the work with a new un-dented plate, T5R5 (thickness 0.125 in), and dented it with a 1.575 inch diameter ball to a deflection of 0.30 inches on the press. We measured the baseline permeability before we dented the plate and then we measured permeability at 0° and 90° after denting and then after annealing at 650°C for 1-1/2 hours. The results are shown in Figure 37. As expected after denting, there is a permeability decrease in the center of the dent which is in compression and there is a ring of higher permeability approximately 1-1/2 inches from the center, which represents tensile stresses. After annealing, the permeability in the center has increased, indicating the compressive stresses have been partially relaxed; however there is a diffuse ring of higher permeability (indicated in yellow) between 1-1/2 and 2 inches from the center of the ring. It is likely that this increase in permeability is due to the geometry changes that are not modeled in the standard permeability/lift-off measurement grids; this effect can be corrected by using modified grids that model the geometry changes. We will pursue an investigation of this effect if we obtain additional funding to characterize pipeline mechanical damage.

Based upon these results and results presented previously, we believe we have demonstrated the feasibility of using permeability C-scans to characterize residual stresses in pipeline mechanical damage sites.

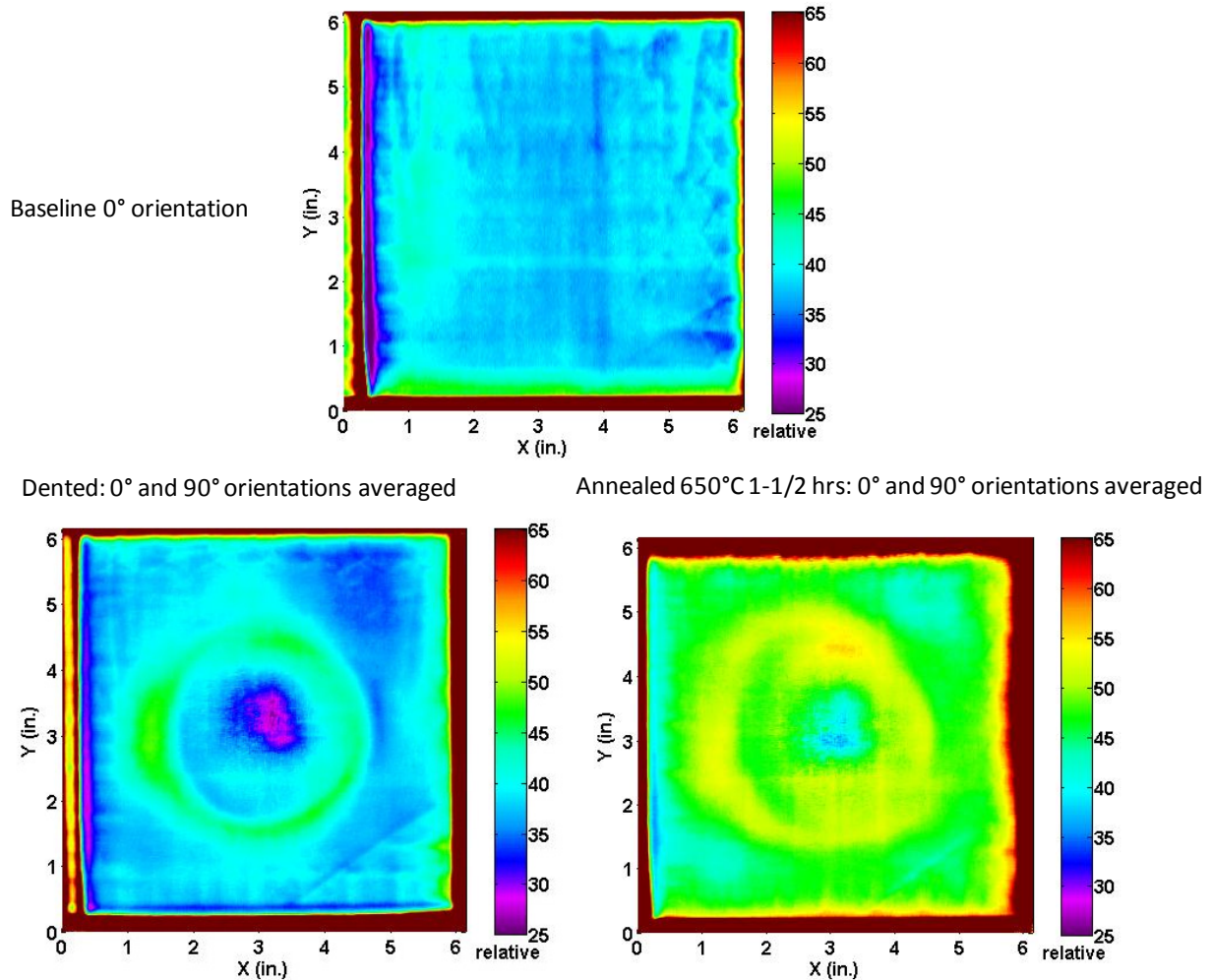
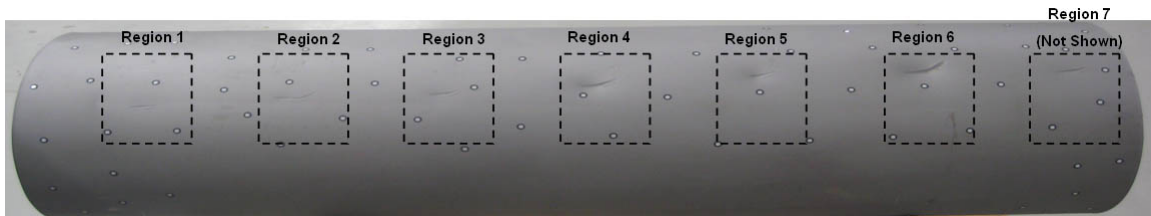


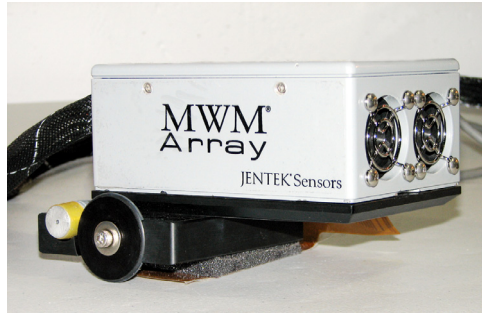
Figure 37. Top; baseline permeability of un-dented plate, bottom left: permeability image from the average of the 0° and 90° permeability images after denting, bottom right: permeability image from the 0° and 90° permeability images after annealing at 650°C for 1-1/2 hours.

3.7 Measurements of mechanical damage on a 16 inch diameter pipe at RTD

Several measurements were performed on a 16-in. diameter pipeline section at RTD that included seven discrete regions of mechanical damage. The damage regions consisted of a combination of dents and gouges and the severity of the damage varied in shapes and sizes. Figure 38a shows the pipeline section and the mechanical damage regions are highlighted. A complete axial scan, over six of the seven damage sites, was performed with an FA24 sensor. The standard manual scanning cart was used. An air-shunt calibration was performed and the data was processed using permeability/lift-off measurement grids. A 0.010-in. thick Mylar shim was placed over the entire length of the pipeline section with regions of mechanical damage. Figure 38b shows a photograph of the probe with the FA24 MWM-Array sensor and the scanning cart used.



(a)



(b)

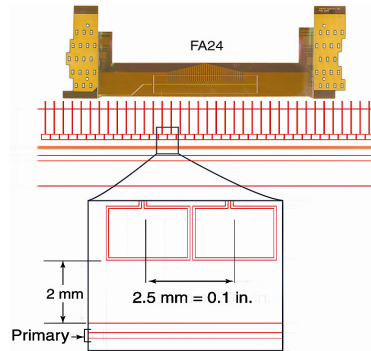


Figure 38. (a) The 5-foot long, 16-in. diameter pipeline section at RTD with seven regions of mechanical damage sites. (b) Pictures of scanning cart and sensor used for these measurements.

Figure 39 shows property images obtained with the FA24 sensor through 0.010-in. clear Mylar sheet. Note that only six of the seven mechanical damage sites are shown on the composite lift-off and permeability scan images. The manual scanning cart has a front wheel encoder and since the seventh region was too close to the edge of the pipeline section, it was difficult to obtain an axial scan of that particular region. Also note that the markers on the pipeline section only appear in the lift-off scan images and not in the permeability scans. This demonstrates reliable independent measurement of lift-off (topography) and permeability (related to residual stress).

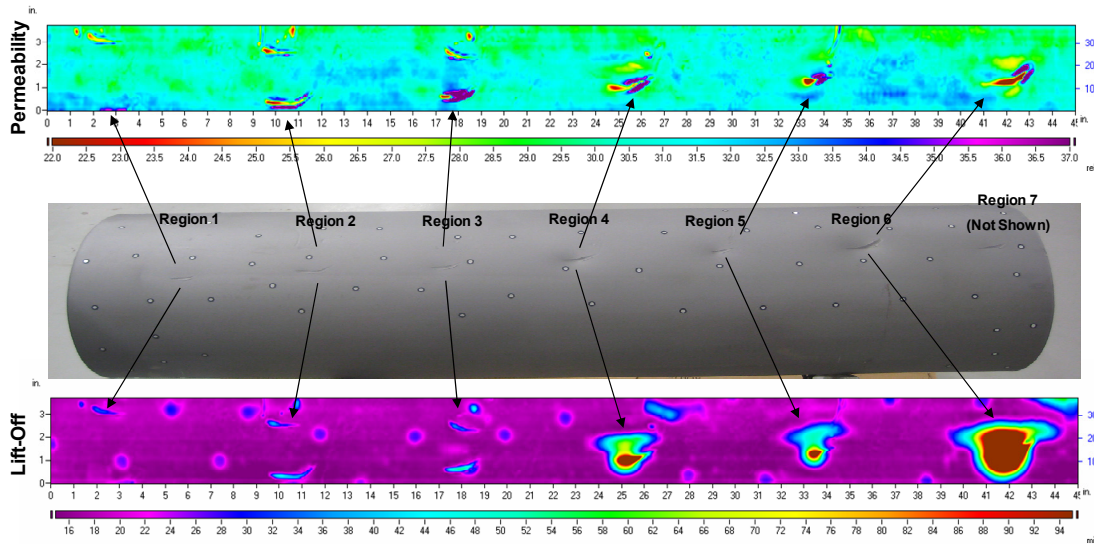


Figure 39. Complete axial scan images of Lift-off (top) and Permeability (bottom) with the FA24 sensor. The mechanical damage regions appear in both the images, although the marker locations are only visible in the lift-off image. The mechanical damage Region 7 is not shown in the property images.

The FA24 sensor was also used to scan over each of the individual regions of mechanical damage. The expanded lift-off and permeability scan images are shown in Figure 40. It should be noted that a single scan was made with the FA24 sensor to obtain the expanded property images.

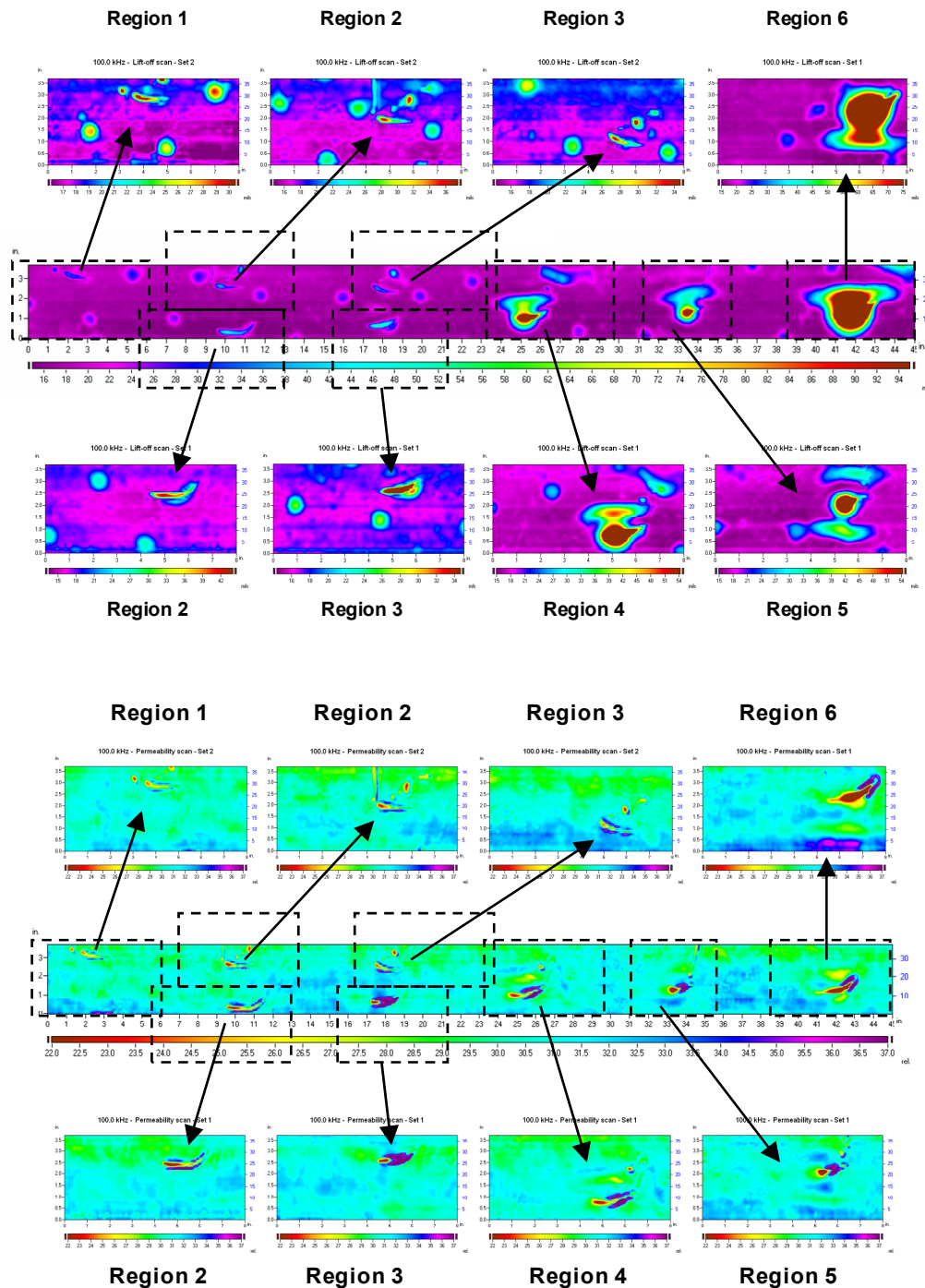


Figure 40. Complete axial scan images of Lift-off (top) and Permeability (bottom) with the FA24 sensor. The mechanical damage regions appear in both images, although the marker locations are only visible in the lift-off image. The mechanical damage Region 7 is not shown in the property images.

Several measurements were then made on the individual mechanical damage regions of the 16-in. diameter pipeline section with the FA26 sensor. The FA26 sensor has the same drive-to-sense distance, but has higher spatial resolution given that its sense elements are 0.05-in., compared to 0.1-in. sense elements for the FA24 sensor. However the width of the scan path of the FA26 sensor is almost half that of the FA24 sensor and hence, two scans were made with the FA26 sensor with several channels of overlap to obtain the expanded property images. Figures 41 to 44 show close-up images of each of the mechanical damage regions as well as the corresponding property images taken with the FA26 sensor. The figures also provide a brief description of each of the regions. All photographs, as well as the data corresponding to size and location of the gouges are provided by Applus/RTD.

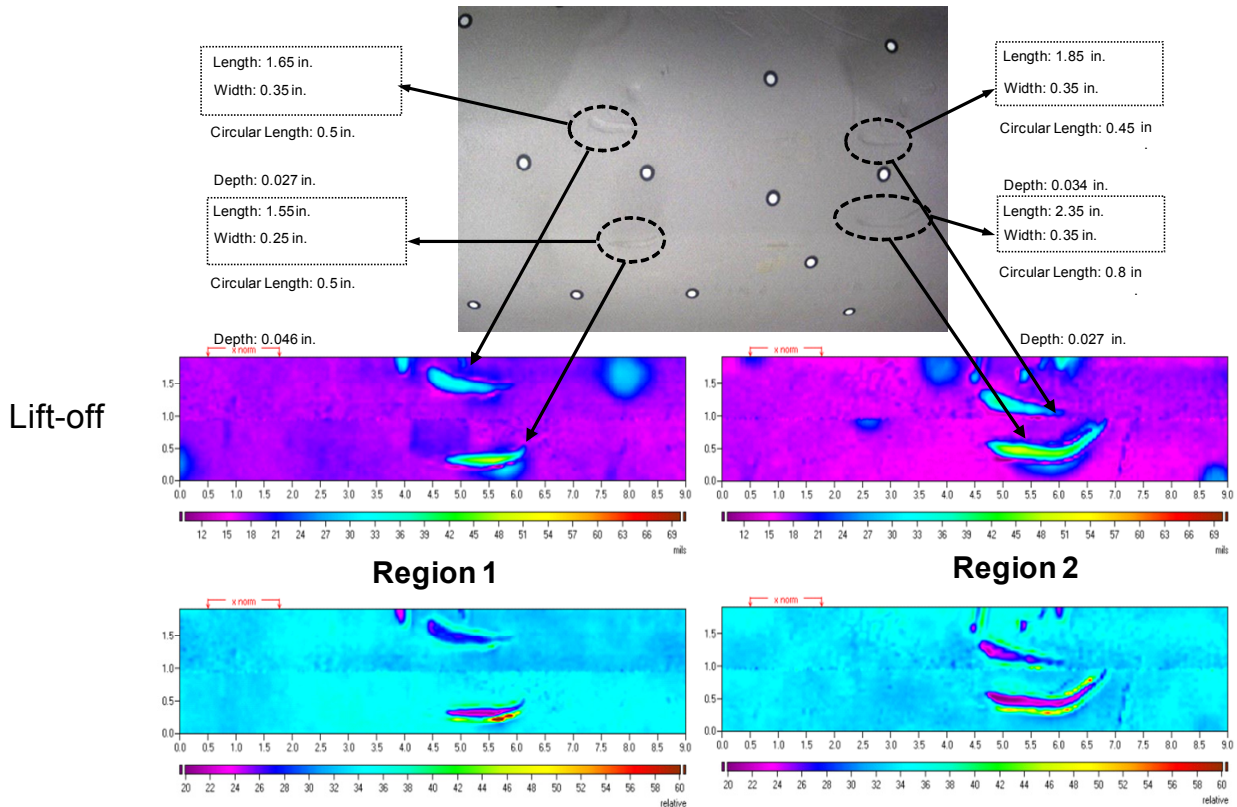


Figure 41. Mechanical damage Regions 1 and 2. Each of the locations contains two gouges. The lift-off images (top) show the marker locations, which are not visible on the permeability images (bottom).

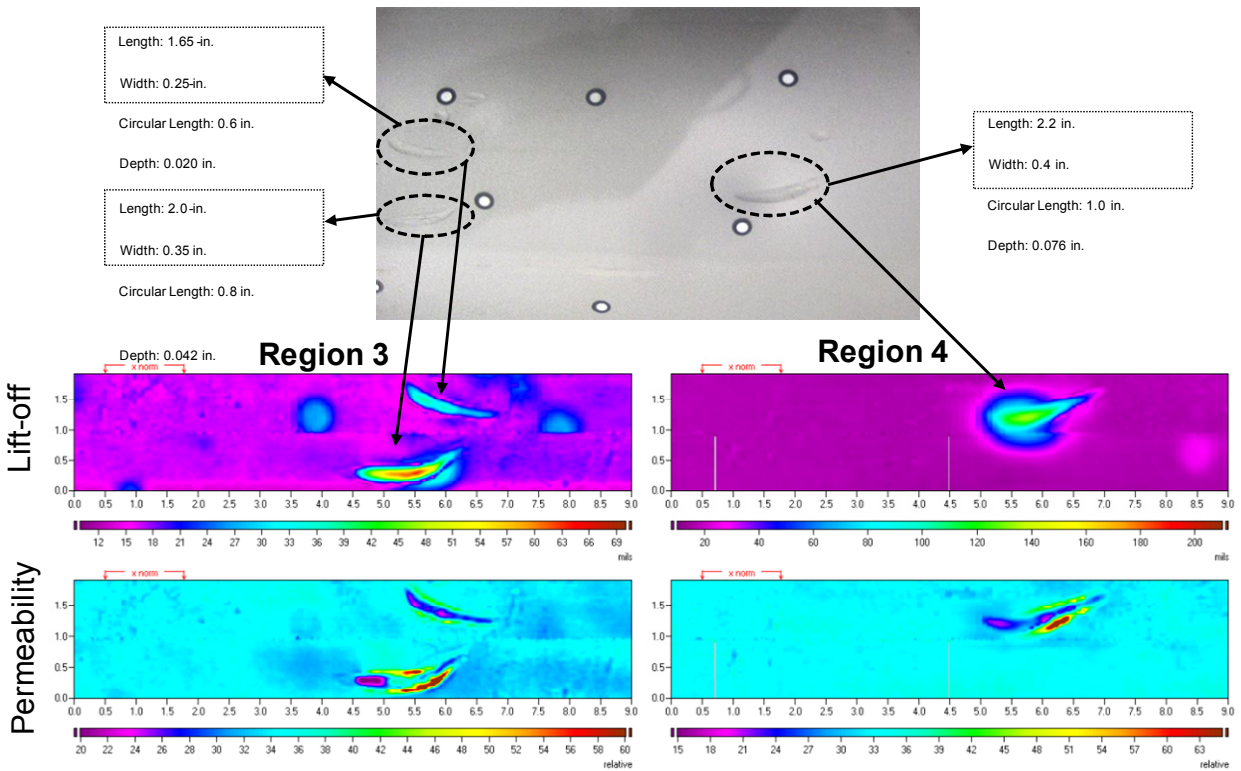


Figure 42. Mechanical damage Regions 1 and 2. Note that Region 3 contains two gouges whereas Region 4 only has one. The lift-off images (top) show the marker locations, which are not visible on the permeability images (bottom).

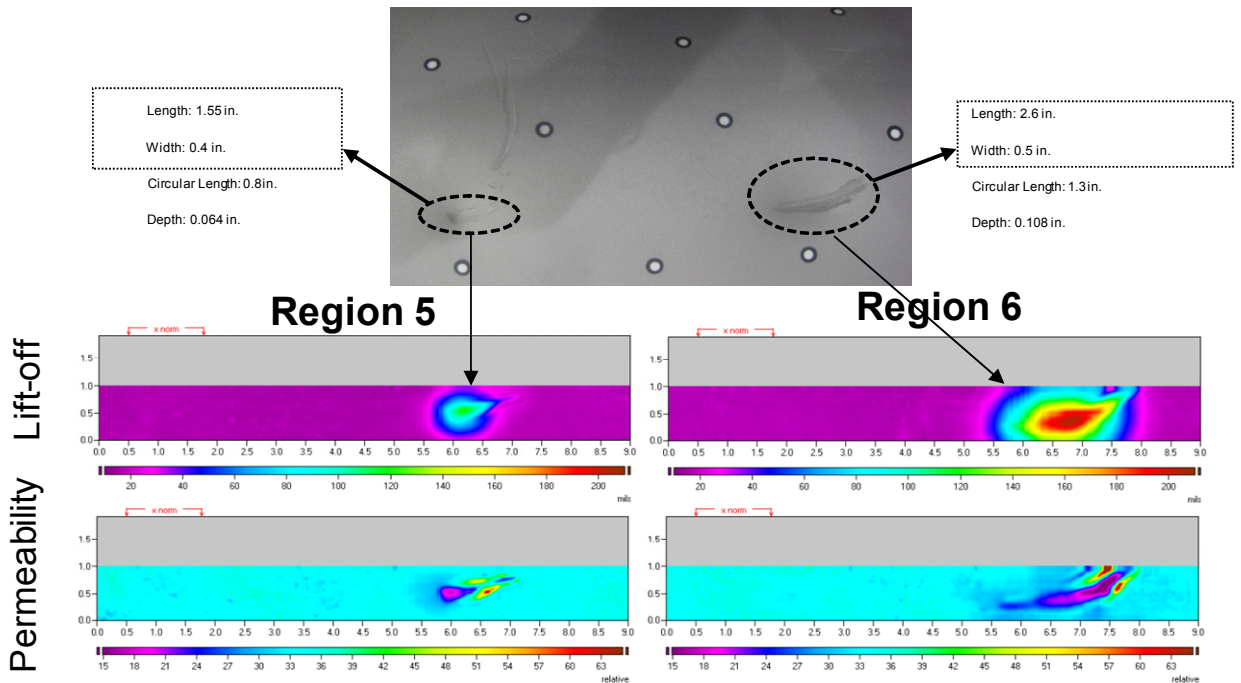


Figure 43. Mechanical damage Regions 5 and 6. Each of the regions only has one gouge.

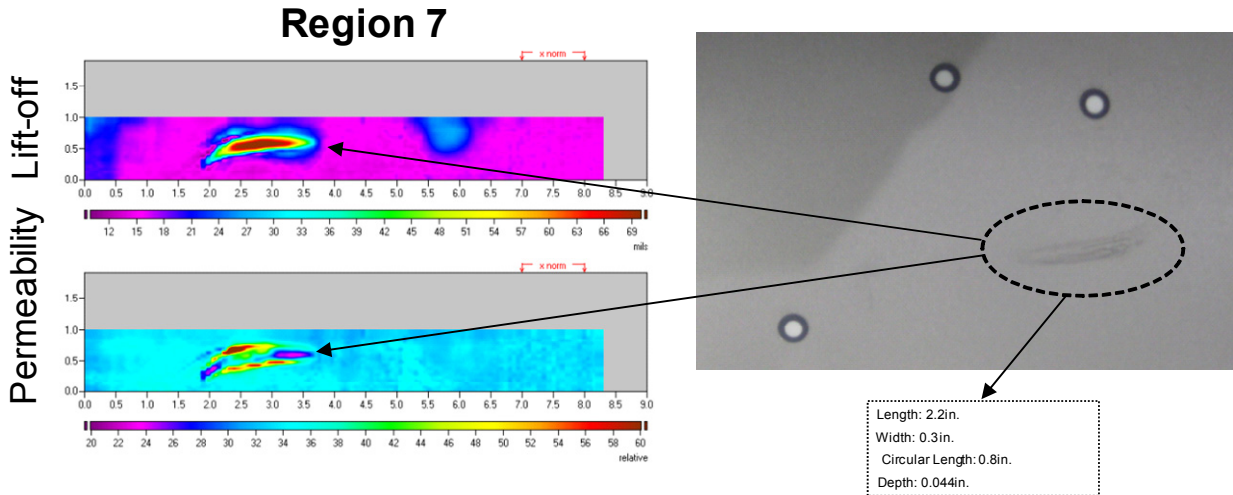


Figure 44. Mechanical damage Region 7. It should be noted that this particular scan with the FA26 sensor was made in the opposite direction (given its close proximity to the edge) from the other scans. Hence, the property images appear flipped compared to the actual photograph of the damage region.

Scans with the FA24 sensor, followed by the FA26 sensor scans illustrate a situation where a sensor with wider coverage can be used, possibly over a moderately thick insulation, followed by a closer inspection with a higher spatial resolution sensor after the coating is removed. The next stage in mechanical damage imaging might be to start quantifying some of the results to obtain a more accurate size and depth estimates. Also, it might be possible to scan the FA24 sensor over a 0.25-in. thick insulation and compare the results to the ones shown in this report. Also, circumferential scans performed with the FA26 sensor might provide more detailed information about the damage sites. We are in the process of modifying our existing fixture to better accommodate circumferential scanning in the near future.

3.8 Measurements of mechanical damage on a 24 inch diameter pipe at RTD

Several measurements were also performed on a 24-in. diameter pipeline section at RTD that included a large plain dent. Figure 45 shows the pipe section and the dent. The dent was at least 1-in. deep at the center and the pipe was deformed over an area several inches in diameter. One set of measurements was performed with the VWA001 sensor that has a 1-in. drive gap. The VWA001 sensor is a larger version of the MWM-Array and is being developed as part of a separate DOT PHMSA program titled “MWM-Array Detection and Characterization of Damage Through Coatings and Insulation.” Although the data taken with this sensor and a prototype scanning fixture are from this separate program, it is presented here to complement the data taken with the FA24 sensor. It also illustrates how the larger VWA001 sensor could be used to inspect for the location and initial characterization of mechanical damage through a coating and the subsequent inspection with an FA24 sensor without a coating (or with a very thin coating) can provide more detailed information about the damage. For this data, an air-shunt calibration was performed and the data was processed using permeability/lift-off measurement grids. A two-inch layer of foam was placed behind the sensor array and used to hold the array against the coated pipe surface.

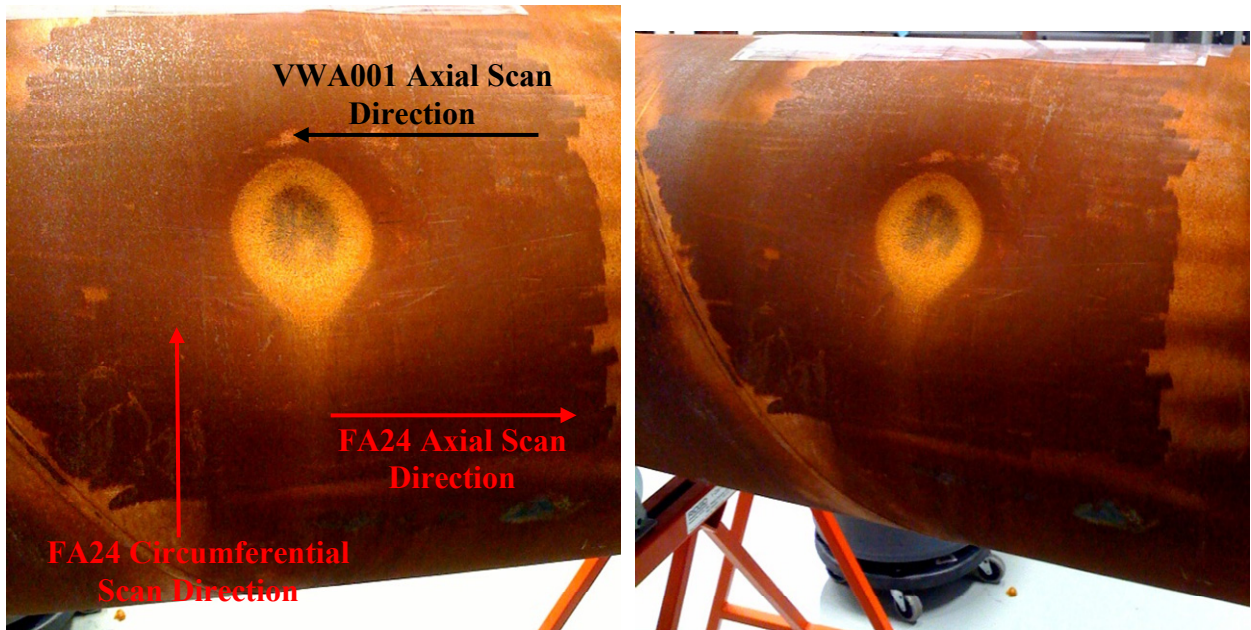


Figure 45. 24-in. diameter pipe section with plain dent. The scan directions for the VWA001 and FA24 MWM-Arrays are indicated.

Figure 46 shows property images obtained with the VWA001 sensor through a 0.25 mm (0.010-in.) semi-rigid insulating sheet. Even though a drive-sense gap of 25.4 mm (1.0-in.) is relatively large for such a thin coating, the nominal coating thickness of approximately 0.25 mm (0.010-in.) was measured with the sensor. Similarly, Figure 47 shows property images obtained with the VWA001 sensor through a 12.7 mm (0.50-in.) semi-rigid insulating sheet of Neoprene rubber which covered the area far from the damage. The MWM array measured lift-off in this area of approximately 12.7 mm (0.5-in.), consistent with the nominal coating thickness. For both coatings, the region of mechanical damage appears as both an increase in the effective lift-off and increase in the relative permeability over a region that is several inches in diameter. The change in lift-off indicates that the depth of the damage is at least 25.4 mm (1.0-in.). This is not the true depth since the measurement grids assumed a planar material geometry and did not account for the geometry of the dent. However, based on other work, this depth is an underestimate of the actual depth of the damage. In the center of the flaw, the data no longer falls on the measurement grids and the property estimates are less reliable; this is most apparent in the 100 kHz data. On the left side of the mechanical damage there is a small decrease in the relative permeability that may be associated with residual stresses in the pipe wall. Thus, a larger wave length VWA sensor would be needed to map the lift-off at the center of this defect.

Figure 48 contains a plot of the effective lift-off for several channels with both coating thicknesses. Note that the channel number is indicated on the right side of each of the scan images in Figure 46 and Figure 47. Channels on the lower portion of the mechanical damage are plotted and show the gradual increase in lift-off associated with the damage. Channel numbers that passed over the center of the damage were not plotted since the data points over the center of the damage did not fall on the measurement grids and the property estimates are not robust. However, these plots show that the measurement procedure, with an air-calibration, correctly provides the nominal coating thickness and the shape of the plots of the mechanical damage are similar for both coating thicknesses. Note that in the future a larger wavelength sensor will be able to address measurements in the center region as well.

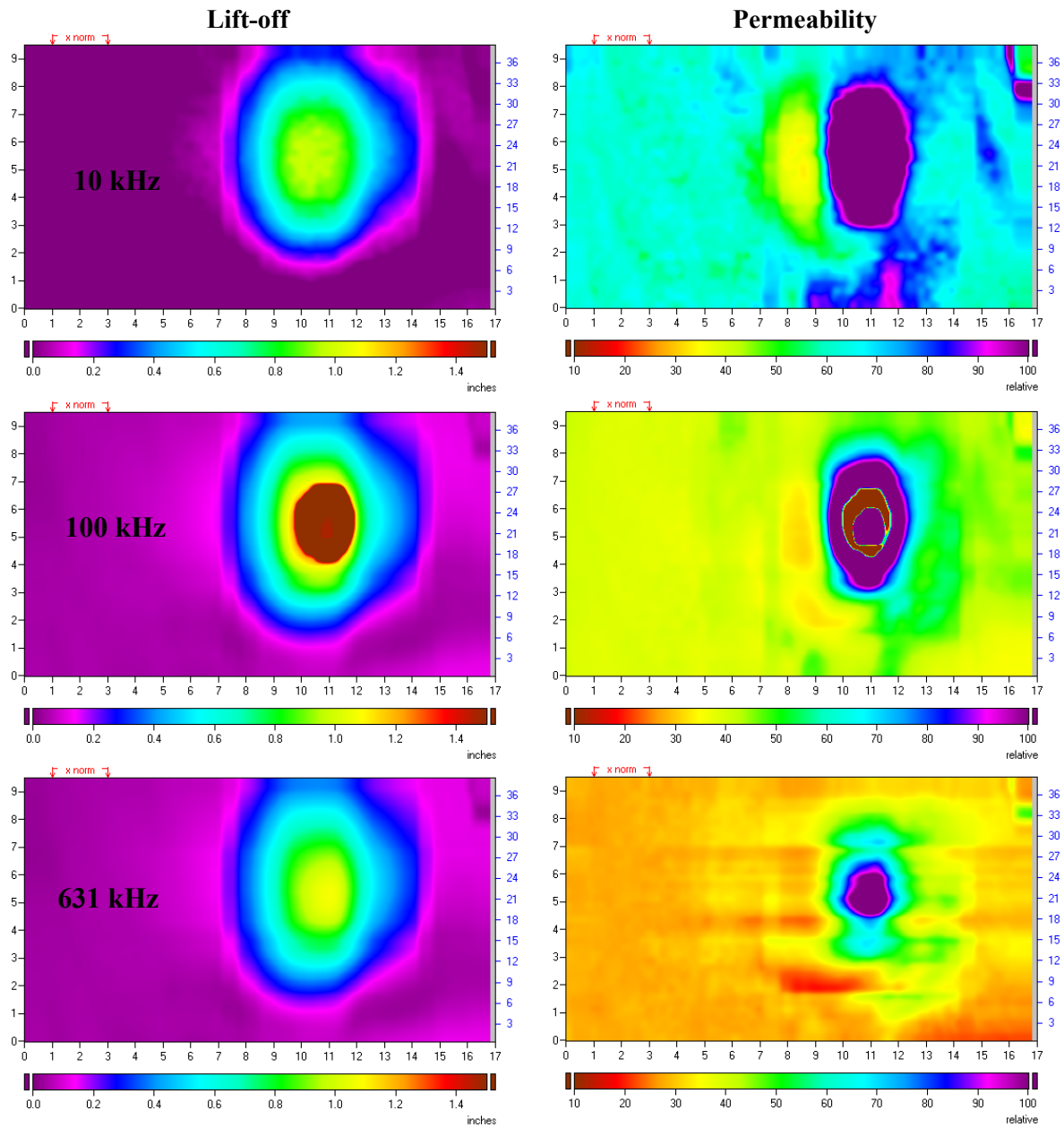


Figure 46. Effective property images obtained with a single pass of a VWA001 sensor with a 25.4 mm (1.0-in.) drive-sense gap and a 0.25 mm (0.010-in.) thick coating.

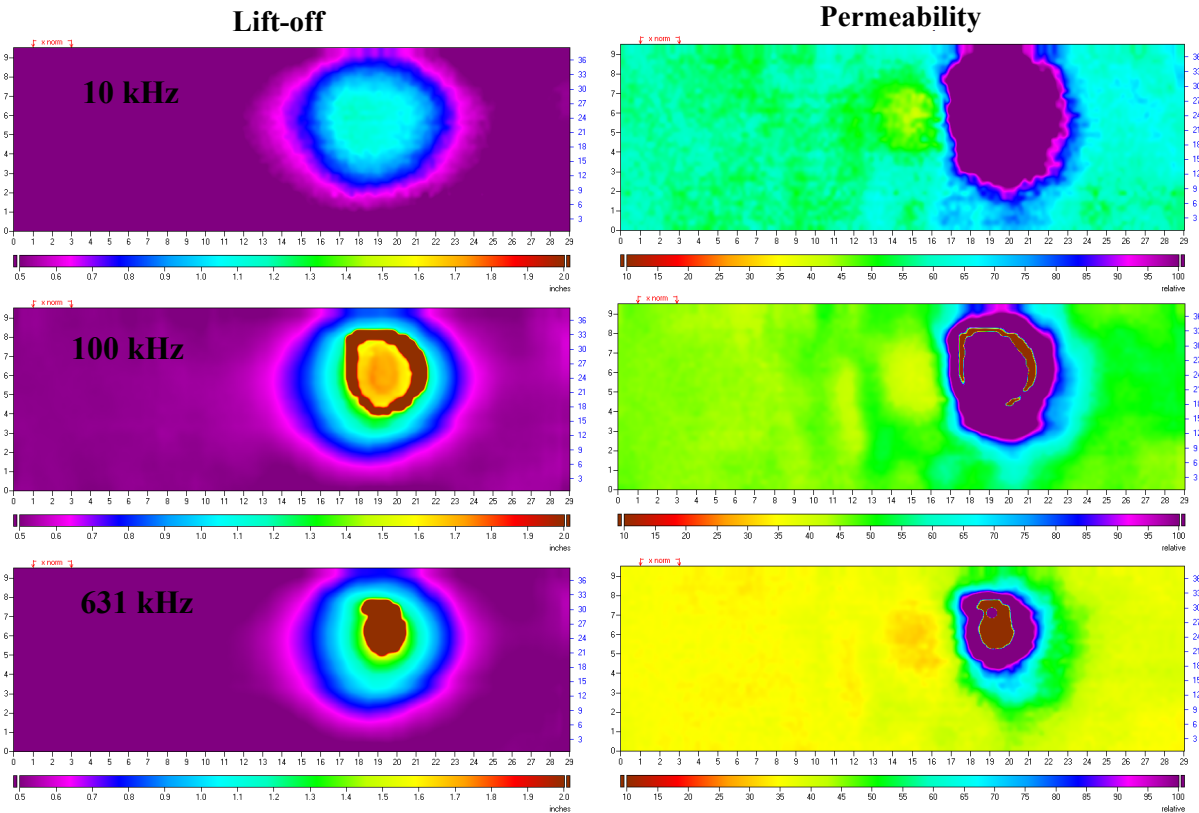


Figure 47. Effective property images obtained with a single pass of a VWA001 sensor with a 25.4 mm (1.0-in.) drive-sense gap and a 12.7 mm (0.50-in.) thick coating.

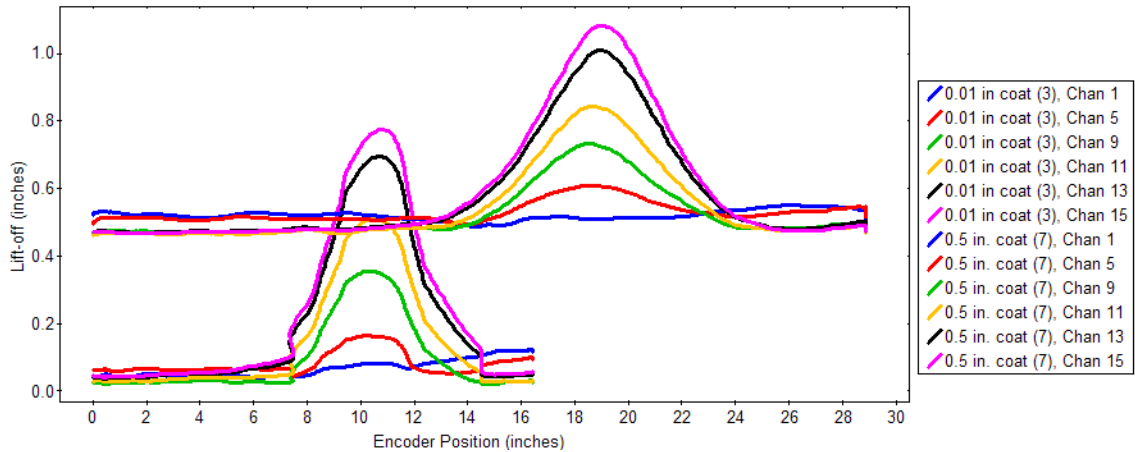


Figure 48. Effective lift-off plots for several channels for two coating thicknesses at 631 kHz.

Measurements were also performed with an FA24 sensor. For these measurements, Kapton tape was placed over the surface of the sensor to protect the sensor. A foam backing behind the sensor array allowed it to conform to the surface of the pipe wall. However, when the sensor array was mounted in the scanning cart, the edges of the cart hit the pipe and prevented the sensor array from conforming to the pipe wall. Consequently, the sensor array was removed from the cart and hand scanned over the surface. Assuming that the scan rate was constant, the measurement number corresponds to the position along the pipe surface. There was an overlap between scans of approximately one-half of the width of the sensor array for building the scan images.

Figure 49 and Figure 50 show effective property images obtained for the axial FA24 sensor. For these scans, the sensor array was scanned in the opposite direction over the dent compared to the scans

performed with the VWA001 sensor. The effective lift-off is approximately constant at a low value of order 0.010-in. except in the vicinity of the central part of the dent. There appears to be some feature, such as surface roughness in the lift-off images, that is consistent with the observed surface finish on the pipe sample. The permeability images show a region of slightly elevated permeability values around the dent and low permeability values within the dent.

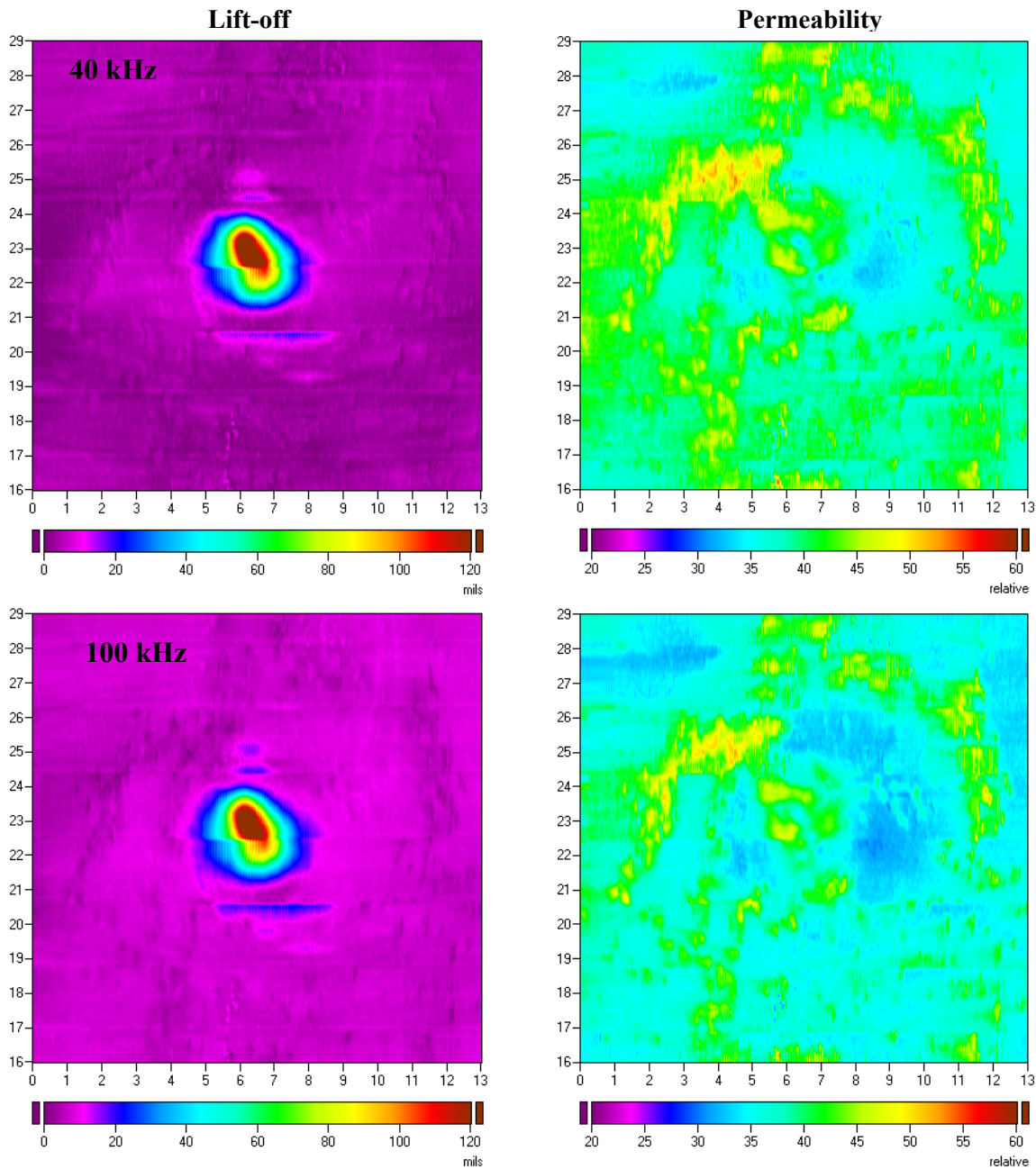


Figure 49. Effective property images obtained with eight (8) passes of an FA24 sensor over the plain dent on the 24-in. diameter pipe section. (Top) 40 kHz. (Bottom) 100 kHz.

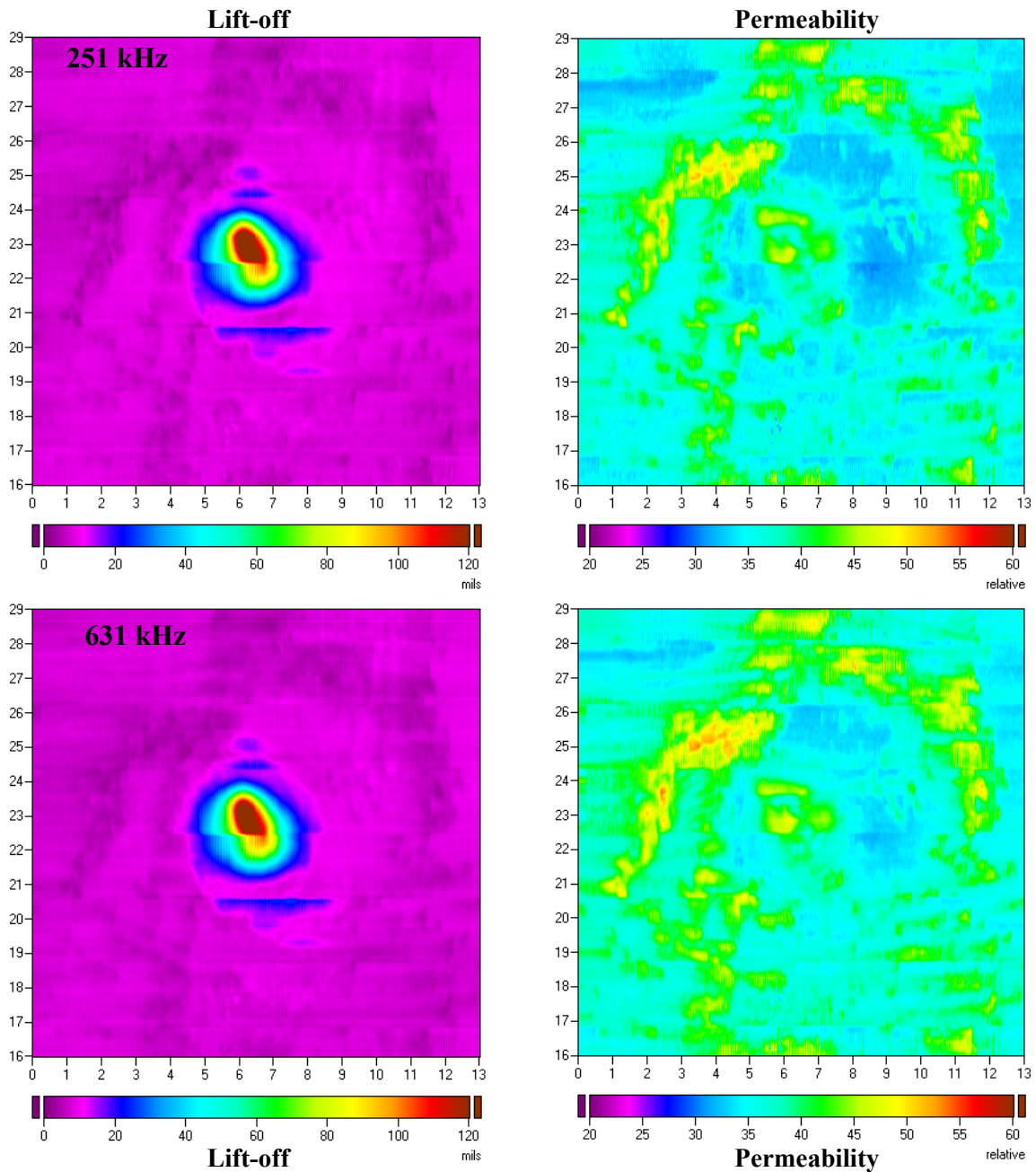


Figure 50. Effective property images obtained with eight (8) passes of an FA24 sensor over the plain dent on the 24-in. diameter pipe section. (Top) 251 kHz. (Bottom) 631 kHz.

Another set of FA24 sensor measurements was obtained using circumferential scans. Again, the cart and position encoder were not useable and the manual-scans were assumed to be performed at a constant scan rate. Figure 51 shows the effective property images obtained for these scans. As with the axial scans, the effective lift-off is approximately constant except in the vicinity of the central part of the dent.

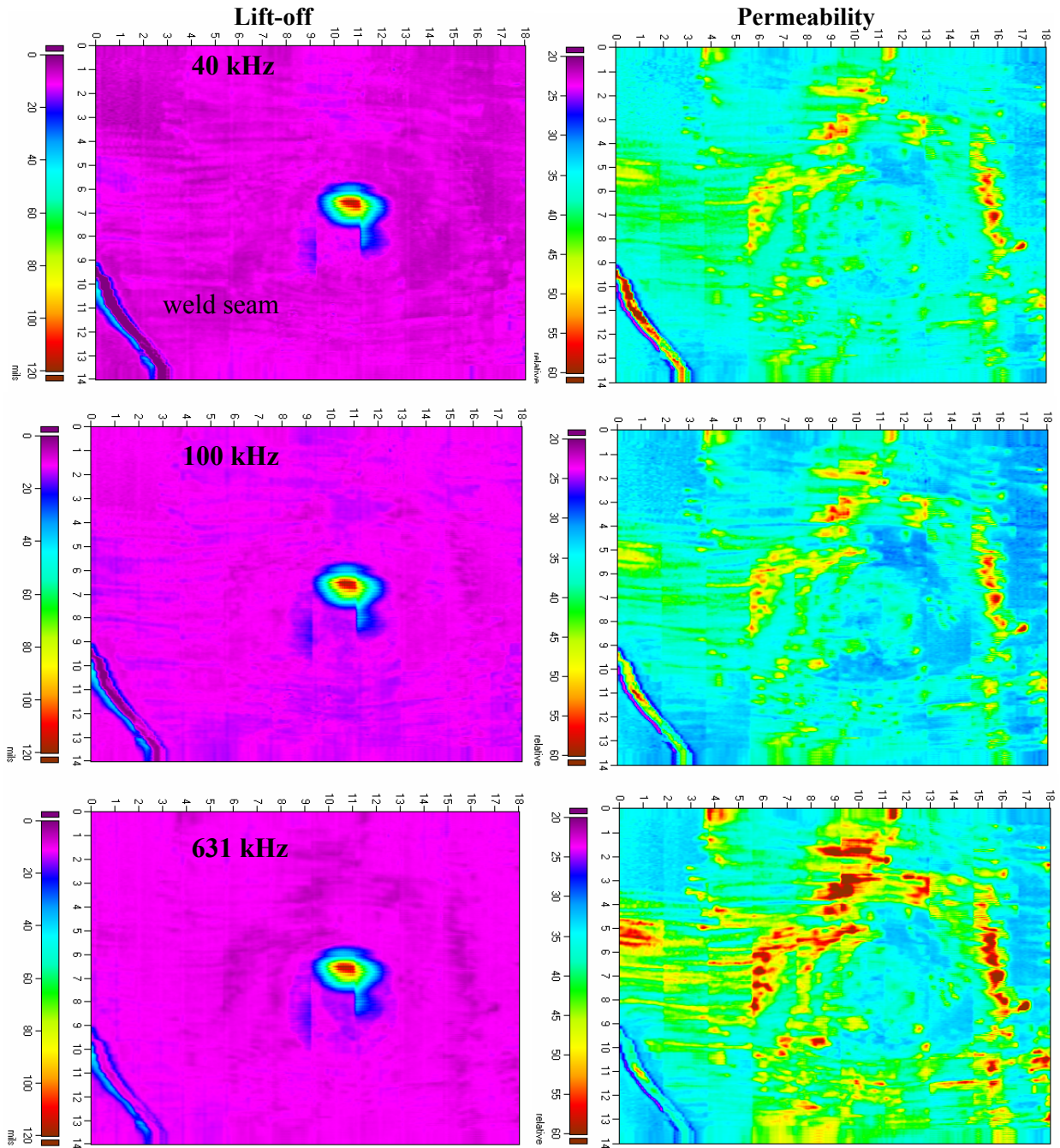


Figure 51. Effective property images obtained with several circumferential scan passes of an FA24 sensor over the plain dent on the 24-in. diameter pipe section. (Top) 40 kHz. (Top) 100 kHz. (Bottom) 631 kHz.

3.9 Changes of electromagnetic properties with strain of selected pipeline steel

Bend specimens made from the ¼-inch thick plate material (4130 steel) that was used for the dent experiments (described previously) were placed in the bend fixture shown in Figure 52. Strain gages were mounted on one side of the specimen. The permeability was measured on the side opposite the strain gages using a single sensing element FS33 sensor (left). The strain was varied from 0 to 1200 μ -strain (approximately 35.5 ksi stress) in 200 μ -strain increments and then decreased back to zero at the same strain increment. The photo on the left of shows the permeability being measured on the tension side of the specimen. To measure the permeability on the compression side, the specimen was flipped and the permeability was measured on the bottom (compression) side of the specimens.

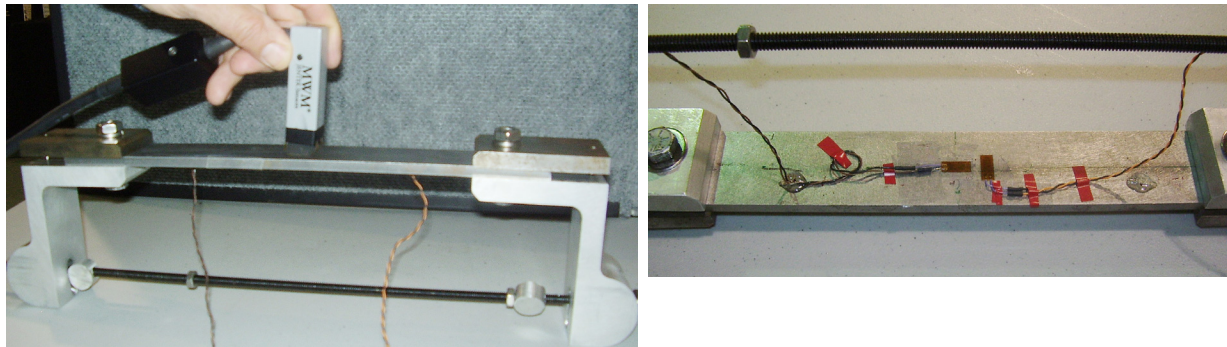


Figure 52. Photo of steel bend specimen showing MWM probe (left) measuring permeability and longitudinal and transverse strain gages (right) for measuring strain.

Figure 53 shows a plot of MWM measured permeability as a function of strain. The permeability increases with tension strain and decreases with compressive strain, as expected for low-alloy steels. The plot also shows there is hysteresis between the loading and unloading permeability measurements, which is expected.

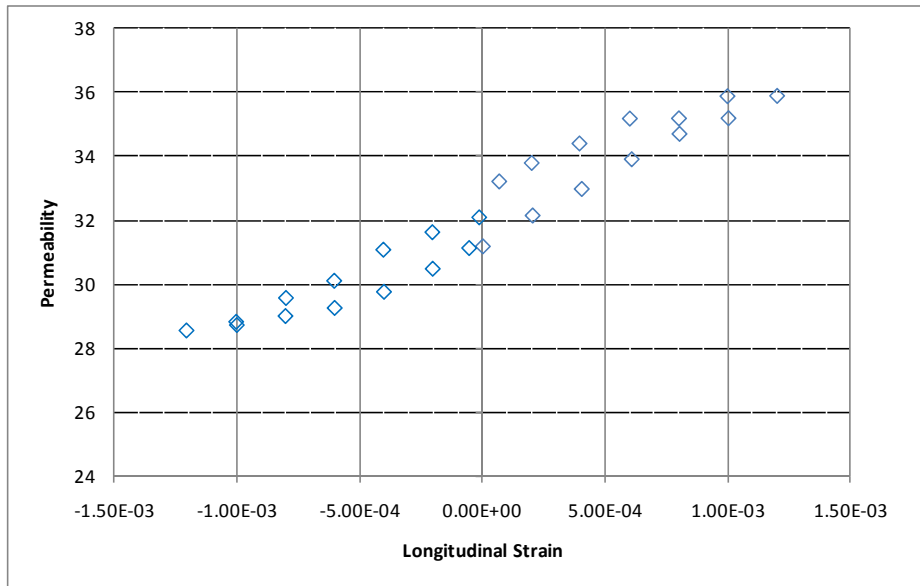


Figure 53. Plot of permeability as a function of strain. Sensor was an FS33 and measurements are at 1 MHz.

Additional characterization of the permeability changes with uniaxial tension and compression stresses on other pipeline steels is recommended as part of a follow on effort. This will help determine if additional relationships between permeability and stress are required for the various steels. It would be useful to know how the pipeline steel type (i.e. X42 versus X100) affects the relationship between permeability and stress. This same approach could be used to determine how stress affects permeability in welds, such as those found in ERW pipelines.

References

1. Baker, M. , “MECHANICAL DAMAGE: Final Report” April 2009, U.S. Department of Transportation under contract DTRS56-02-D-70036.
2. Clapham, L., Babbar, V., Byrne, J., Queen’s University, Kingston, Ontario, Canada. “Detection of Mechanical Damage Using the Magnetic Flux Leakage Technique.”